Princeton Plasma Physics Laboratory

PPPL-

PPPL-

PPPL
PRINCETON PLASMA
PHYSICS LABORATORY

Princeton Plasma Physics Laboratory
Report Disclaimers

PPPL Report Availability

Princeton Plasma Physics Laboratory:

http://www.pppl.gov/techreports.cfm

Office of Scientific and Technical Information (OSTI):

http://www.osti.gov/bridge

Related Links:

U.S. Department of Energy

Office of Scientific and Technical Information

Fusion Links

Mode conversion of Langmuir to electromagnetic waves with parallel inhomogeneity in the solar wind and the corona

Eun-Hwa Kim,* Iver H. Cairns, and Peter A. Robinson

School of Physics, University of Sydney, New South Wales 2006, Australia

(Dated: June 3, 2008)

Linear mode conversion of Langmuir waves to radiation near the plasma frequency at density gradients is potentially relevant to multiple solar radio emissions, ionospheric radar experiments, laboratory plasma devices, and pulsars. Here we study mode conversion in warm magnetized plasmas using a numerical electron fluid simulation code with the density gradient parallel to the ambient magnetic field $\mathbf{B}_0$ for a range of incident Langmuir wavevectors. Our results include: (1) Both o- and x-mode waves are produced for $\Omega \propto (\omega L)^{1/3}(\omega_c/\omega) \lesssim 1$, contrary to previous ideas. Only o mode is produced for $\Omega \gtrsim 1.5$. Here ω_c is the (angular) electron cyclotron frequency, ω the angular wave frequency, and L the length scale of the (linear) density gradient. (2) In the unmagnetized limit, equal amounts of o- and x-mode radiation are produced. (3) The mode conversion window narrows as Ω increases. (4) As Ω increases the total electromagnetic field changes from linear to circular polarization, with the o- and x- mode signals remaining circularly polarized. (5) The conversion efficiency to the x mode decreases monotonically as Ω increases while the o-mode conversion efficiency oscillates due to an interference phenomenon between incoming and reflected Langmuir/z modes. (6) The total conversion efficiency for wave energy from the Langmuir/z mode to radiation is typically less than 10%, but the corresponding power efficiencies differ by the ratio of the group speeds for each mode and are of order $50 - 70\%$. (7) The interference effect and the disappearance of the x mode at $\Omega \gtrsim 1$ can be accounted for semiquantitatively using a WKB-like analysis. (8) Constraints on density turbulence are developed for the x mode to be generated and be able to propagate from the source. (9) Standard parameters for the corona and the solar wind near 1 AU suggest that linear mode conversion should produce both o- and x- mode radiation for solar and interplanetary radio bursts. It is therefore possible that linear mode conversion under these conditions might explain the weak total circular polarizations of type II and III solar radio bursts.

I. INTRODUCTION

Standard linear analyses of dispersion equations for homogeneous plasmas yield wave modes that are uncoupled and distinct. However, in inhomogeneous plasmas the wave modes are often coupled to each other. For some range of frequencies and angles of propagation, the energy then can be transformed linearly from one mode to another with constant frequency via processes called linear mode conversion (LMC) [1].

Magnetoionic theory describes the free-space electromagnetic (EM) ordinary (o) and extraordinary (x) modes with opposite circular polarizations, the mixed Langmuir and z modes (termed the Langmuir/z mode below), and the whistler mode. The restricted ranges of wavevector and frequencies for which LMC can proceed are termed "radio windows " [2, 3]. Two are widely discussed for the o and Langmuir/z modes. The first radio window is for Langmuir/z waves with frequency just above the local plasma frequency (f_p) and wave vectors close to parallel to the ambient magnetic field ($\mathbf{B}_0$) direction. The second involves wavevectors almost perpendicular to $\mathbf{B}_0$ and frequencies close to the upper hybrid frequency (f_{uh}). This

paper concentrates on the first radio window for conversion of Langmuir/z waves into radio emission, expanding in detail on a recent demonstration [4] that both o and x-mode radiation can be produced. A similar but inverse mechanism may also partially convert incoming o-mode and x-mode waves into Langmuir waves [2, 3].

Mode conversion from Langmuir/z waves into EM radiation is illustrated in Figure 1 for both unmagnetized and magnetized plasmas. In unmagnetized plasmas, when a Langmuir wave propagates in the direction of increasing plasma density, it can reach a critical point (Z_{mc}) where the wave frequency is equal to f_p. Near this mode conversion point the wave is partially reflected by the density profile and partially converted into EM waves.

The problem becomes significantly more complex in magnetized plasmas. When Langmuir/z waves propagate up or down a longitudinal density gradient, they encounter Z_{mc}. They also encounter the points where the cutoffs of the o (Z_{cut}^o) and x modes (Z_{cut}^x) occur, located on the underdense side and lower down the density gradient than Z_{mc}, whereas the z-mode cutoff (Z_{cut}^z) occurs on the overdense side higher up the density gradient than Z_{mc}. A Langmuir/z-mode wave can propagate from the low density region through Z_{mc}, turn back at Z_{cut}^z, and then propagate back toward the lower density region. In principle LMC can occur partially on both the way in and the way out. The converted EM energy is then ex-

*Now at Princeton Plasma Physics Laboratory; Electronic address: ehkim@pppl.gov

pected to propagate independently in the o and x modes out of the coupling region to the underdense side.

LMC from Langmuir/z mode into EM waves is potentially relevant to radiation from foreshock regions upstream of Earth's bowshock [5, 6], type II and III radio bursts from the solar corona and interplanetary medium [3, 7], and radiation from the outer heliosphere [8], which involve the conversion into radio emission near f_p and/or $2f_p$ of Langmuir energy extracted from electron beams. LMC is also believed important in producing auroral roar emissions [9] and pulsar radiation [10]. LMC of incoming EM waves into Langmuir/z waves is relevant to heating of laboratory plasmas [11], ionospheric modification and radar experiments [12], and laser experiments on surface plasmon resonance [13].

Nonlinear conversion mechanisms have also been proposed to account for f_p and $2f_p$ radiation [3, 14]. For instance, $2f_p$ radiation in type II and III bursts and from Earth's foreshock can be produced by the nonlinear coalescence process $L + L' \leftrightarrow T$ ($2f_p$) [14]. Moreover, nonlinear processes can yield radiation near f_p, due to scattering of Langmuir waves off thermal ions or various three-way decay and coalescence processes [15]. Early workers favored nonlinear mechanisms due to the very highly nonthermal levels of Langmuir waves involved and because calculations suggested that the efficiency of LMC was inadequate. However, subsequent calculations for 1-D linear density gradients yield (power) conversion efficiencies $\epsilon \approx 50 - 70\%$ in a narrow angular window dependent on the properties of incoming Langmuir/z waves and density structures [16–23]. It was found that in magnetized plasmas ϵ slightly decreases and the mode conversion window becomes narrower compared with unmagnetized calculations [16, 19]. More recently, assuming 2-D and 3-D density irregularities, Cairns and Willes [25] averaged ϵ over plausible distributions of the (vector) density gradient and Langmuir wavevector and showed that the averaged 3-D efficiency is $10^{-6} - 10^{-5}$ for plausible solar wind and coronal parameters. These values are similar to the nonlinear conversion efficiencies calculated theoretically and found to plausibly account for observed type III solar radio bursts [15, 26]. At present, one major theoretical issue is thus whether LMC or nonlinear processes dominate in producing solar, interplanetary, foreshock, and outer heliospheric emissions. Further investigations of LMC are therefore necessary.

Another unresolved theoretical issue is the partial polarization of f_p emission in type II and III bursts, which have degrees of polarization between 0 and 70% and are never 100% polarized [27] (usually $< 10\%$ for type IIs). The problem is that existing theories for LMC and nonlinear processes predict that f_p emission should be 100% polarized in the sense of the o mode [2, 3, 5, 16, 28]. There are two possibilities for explaining partial polarization of f_p: either the lower polarization is intrinsic to the source region (and so the emission mechanism) or the radiation is depolarized as a propagation effect. Since lower intrinsic polarization can occur only if the initial

frequency exceeds the x-mode cutoff frequency (f_{cut}^x), the previous expectation that LMC and nonlinear processes would produce only o-mode radiation meant that depolarization theories were mainly investigated. These include mode coupling [29], scattering by low frequency waves [30, 31], and reflection at density inhomogeneities [32]. However, Mjølhus [20] showed that an incident x-mode wave perpendicular to $\mathbf{B}_0$ can undergo LMC into an ES wave and a reflected x-mode wave at ionospheric density irregularities. Similarly, in laboratory plasmas, LMC of x mode to ES energy is one method to inject energy into an overdense plasma [33]. The relevance is that if LMC can occur from the Langmuir/z mode to both the x mode and the o mode near f_p, then the partial polarizations of type II and III bursts can potentially be explained without depolarization theories.

Recently Kim et al. [4] have demonstrated that LMC can indeed produce x-mode as well as o-mode radiation from Langmuir/z waves, contrary to earlier expectations of the o-mode only [2, 3, 5, 16]. They solved the full wave equations numerically using a fluid simulation code. The code studies Langmuir/z waves approaching a linear density gradient from a region with constant density, as well as the o, x, and Langmuir/z mode waves that leave this region, extending the approach of Willes and Cairns [21]. Many earlier analyses focused solely on calculating the total conversion efficiency [18–20, 22, 23], which may be determined without resorting to a full wave field solution, or introduced approximate analytic simplifications. When the waves propagate quasi-parallel to $\mathbf{B}_0$ both the o and x modes have electric components perpendicular to $\mathbf{B}_0$. Thus it is necessary to calculate the full wave field solution to demonstrate whether outgoing EM waves are purely o mode or not.

The overall aims of this paper are to demonstrate that Langmuir/z- mode waves can be converted into x-mode and o-mode radiation by LMC when the density gradient L is parallel to $\mathbf{B}_0$ and to calculate the mode conversion efficiency for different angles of propagation, density scale lengths, and magnetic field strength. This involves extending and expanding on the work of Ref. [4] using the same numerical approach. There are multiple subsidiary aims. First, to show that LMC can be significant and produce approximately equal amounts of o- and x-mode waves in the unmagnetized and weakly magnetized limits, but with only the o mode produced at sufficiently high magnetization. Second, to show that production of both o and x radiation should occur for typical solar wind and coronal parameters, naturally alleviating the depolarization problem for solar radio bursts. Third, to explore how the conversion efficiencies into the o and x modes vary with the properties of the waves and plasma. Fourth, to show that the oscillations in the o-mode conversion efficiency can be explained semiquantitatively as an interference phenomenon. Fifth, to calculate the transmission factor for energy tunneling along various evanescent connecting modes in the mode conversion window, so as to to model semiquantitatively LMC for the o and x modes.

Sixth, to show that the transmission factors predict that the x and o modes should have essentially identical conversion efficiencies under unmagnetized and weakly magnetized conditions, with zero x mode at sufficiently high magnetization. Seventh, to use the transmission factors to explain semiquantitatively why the x-mode efficiency decreases monotonically with increasing magnetization and does not experience interference effects. Eighth, to predict the net degree of polarization, based on simulations and theoretical transmission factors, as well as the level of density fluctuations required for the x mode to propagate. Ninth, to explore possible applications of LMC to solar radio bursts in the solar wind at 1AU and the coronal region, finding that the x mode should be produced under reasonable conditions and that the net polarization could be consistent with either the o or x mode depending on the detailed plasma parameters.

This paper is structured as follows: The numerical simulation code is described in Section II. Section III contains simulation results such as the dependence of the electric field and the hodograms on magnetization and the density gradient. They show direct evidence for production of both the x and o modes, with efficiencies that vary with the plasma and inhomogeneity parameters. The mode conversion efficiency ϵ is presented in Section IV. From the simulation data, we determine the power of the incoming and reflected Langmuir$/z$ waves and outgoing EM waves, and calculate the mode conversion efficiency. The dependence of the mode conversion efficiency on the Langmuir$/z$ wave incidence angle and the ambient magnetic field strength are also described. In Section V, the coupling of Langmuir$/z$ waves into EM waves in an inhomogeneous plasma is calculated numerically using analytic plasma theory. The transmission factors for the o, x, and evanescent coupling modes are calculated and discussed, together with the net degree of polarization of the outgoing EM waves and the level of density fluctuations required for the x mode to be produced and propagate from the source. Possible applications of LMC to solar radio bursts in the solar wind at 1AU and the coronal region are described in some detail in Section VI. The last section contains a brief discussion and the conclusions.

II. NUMERICAL MODELING

To investigate LMC between Langmuir and EM waves in warm magnetized plasmas, we use the numerical fluid simulation code developed by Kim et al. [4]. It solves the linearized Maxwell equations, the electron momentum and continuity equations for an electron fluid with finite mass and thermal pressure, and Ohm's law:

$$\nabla \times \mathbf{E} = -\frac{\partial \mathbf{B}}{\partial t}, \tag{1}$$

$$\nabla \times \mathbf{B} = \mu_0 \mathbf{J} + \frac{1}{c^2}\frac{\partial \mathbf{E}}{\partial t}, \tag{2}$$

$$N_0 m_e \frac{\partial \mathbf{v}}{\partial t} = -N_0 e(\mathbf{E} + \mathbf{v} \times \mathbf{B}_0) - ne\mathbf{E}_0 - \nabla p, \tag{3}$$

$$\frac{\partial n}{\partial t} = -N_0 \nabla \cdot \mathbf{v}, \tag{4}$$

$$\mathbf{J} = -N_0 e\mathbf{v}. \tag{5}$$

Here $\mathbf{E}$, $\mathbf{B}$, $\mathbf{v}$, and $\mathbf{J}$ are the perturbed electric and magnetic fields, electron velocity, and current density, n and p are the perturbed electron density and pressure, and N_0, $\mathbf{E}_0$, and $\mathbf{B}_0$ are the background electron density, and electric and magnetic fields, respectively. Note that only linear perturbations are contained in Eqs. (1) - (5). Accordingly only linear conversion processes are studied and nonlinear processes are not included.

The plasma is assumed to obey an adiabatic pressure law with $PN^{-\gamma} =$constant, where P and N are the plasma pressure and density, respectively, and γ is the ratio of specific heats. For small perturbations, $P_0 = N_0 T_0$ and $p = \gamma n P_0 / N_0$, where T_0 and P_0 are the background electron temperature and pressure. The pressure force associated with the density gradient is balanced by a steady state ambipolar electric field $\mathbf{E}_0$. From the electron momentum equation, $\mathbf{E}_0$ can be calculated as

$$\mathbf{E}_0 = -\frac{\nabla P_0}{N_0 e}. \tag{6}$$

In order to solve Eqs. (1) - (5) numerically, the model of Figure 2 and the following assumptions are adopted:

1. $\mathbf{B}_0$ and ∇N_0 lie in the Z direction and B_0 is constant. We define $X_e = f_p^2/f^2$ with

$$X_e(Z) = X_0 \quad \text{for} \quad Z \leq 0 \tag{7}$$
$$= X_0(1 + Z/L) \quad \text{for} \quad Z > 0 . \tag{8}$$

Here $X_0 = X_e(0) = f_{p0}^2/f^2$, L is the dimensionless density length scale, and f is the wave frequency. The nominal mode conversion point Z_{mc} is defined by $X(Z_{\mathrm{mc}}) = 1$ (equivalent to Z_{cut}^o when $K_X = K$).

2. All variables vary as $\mathbf{A} = A(Z,t)\exp(iK_X X)$ where X, Z, and K_X are normalized lengths and wavenumbers: $X = k_0 x$, $Z = k_0 z$, $K_X = k_x/k_0$, and $k_0 = 2\pi f/c = \omega/c$. Here K_X is constant by Snell's law and, for simplicity, we assume $K_Y = 0$ without loss of generality.

3. Langmuir waves are generated in Region II of Figure 2 with f and wavevector $(K_X^L, 0, K_Z^L)$ related by the dispersion relation in a warm magnetized plasma.

4. Typical solar wind values for the electron density $(2\pi f_{p0} = \omega_{p0} = 2 \times 10^5 \text{ s}^{-1})$ and density scale length $(k_0 L = 1 \times 10^3)$ are used.

5. The temperature dependence on ϵ is very weak. For instance Figure 1 in Ref [17] showed that reducing v_{th}^2/c^2 from 0.1 to 0.005 changes the peak efficiency by $< 5\%$ and that the maximum difference is less than 50% for any K_X at the same $k_0 L$. They also showed that the cold plasma prediction is essentially equal to the results for $v_{th}^2/c^2 = 0.005$. Thus, in order to save computing time, we assume that $\gamma v_{th}^2/c^2 = 0.01$ rather than the more plausible value of $10^{-4} - 10^{-5}$ for the corona and solar wind.

6. Damping is included in Region I and the leftmost boundary absorbs all waves.

For $k_0 L \gg 1$ and $X_0 = 0$, ϵ is expected to be primarily a function of the quantities [17, 19]

$$q = (k_0 L)^{2/3} \sin^2 \theta_{\text{in}}^L, \tag{9}$$

$$\Omega = (k_0 L)^{1/3} \sqrt{Y}, \tag{10}$$

where θ_{in}^L is the incidence angle of Langmuir waves, $Y = \omega_c/\omega$, and ω_c is the electron gyrofrequency. Willes and Cairns [21] generalized Eq. (9) to $X_0 \neq 0$ in the unmagnetized limit, finding that ϵ is primarily a function of

$$q = (k_0 L)^{2/3} K_\perp^2$$
$$= (k_0 L)^{2/3} \frac{\mathcal{P}_e}{\gamma \beta} \sin^2 \theta_{\text{in}}^L, \tag{11}$$

where $K_\perp$ is the component of the wavevector perpendicular to $\mathbf{B}_0$, $\mathcal{P}_e = 1 - X_0$, and $\beta = T_0/m_e c^2$. Predictions for the maximum value of θ_{in}^L can be derived as follows, extending an earlier analysis [21]. The maximum values of q for mode conversion to the o and x modes are defined by $\sin^2 \theta_{\text{out}}^o = 1$ and $\sin^2 \theta_{\text{out}}^x = 1$, where θ_{out}^o and θ_{out}^x are angles between $\mathbf{B}_0$ and the outgoing o- and x-mode wavevectors. Under these conditions, the outgoing waves propagate perpendicular to $\mathbf{B}_0$. For small $K_\perp$, the phase speeds of the o and x modes are much larger than v_{th}, and the dispersion relations of the o and x modes are reduced approximately to those for cold plasma theory:

$$(K_\perp^o)^2 \cong \mathcal{P}_e, \tag{12}$$

$$(K_\perp^x)^2 \cong \mathcal{R}_e \mathcal{L}_e / \mathcal{S}_e, \tag{13}$$

where $\mathcal{R}_e = 1 - X_0/(1 - Y)$, $\mathcal{L}_e = 1 - X_0/(1 + Y)$, and $\mathcal{S}_e = (\mathcal{R}_e + \mathcal{L}_e)/2$. Noting that $K_\perp$ for the incoming Langmuir/z wave is identical to that for the outgoing EM wave, Eqs. (11) - (13) impose a maximum angle θ_{max}^L between the Langmuir/z wavevector and $\mathbf{B}_0$ for mode conversion to occur. Specifically, the angles θ_{max} for mode conversion from Langmuir/z to the o and x modes are predicted to be

$$\theta_{\text{max}}^o \cong \sin^{-1} \sqrt{\gamma \beta}, \tag{14}$$

$$\theta_{\text{max}}^x \cong \sin^{-1} \sqrt{\gamma \beta \frac{\mathcal{R}_e \mathcal{L}_e}{\mathcal{S}_e \mathcal{P}_e}}. \tag{15}$$

The maximum values of q for the o mode and x mode are also derived from (11) - (13) as

$$q_{\text{max}}^o \cong (k_0 L)^{2/3} \mathcal{P}_e, \tag{16}$$

$$q_{\text{max}}^x \cong (k_0 L)^{2/3} \mathcal{R}_e \mathcal{L}_e / \mathcal{S}_e. \tag{17}$$

Figure 3 shows θ_{max} and q_{max} as a function of Ω for $\omega_p = 2 \times 10^5$ s^{-1}, $k_0 L = 1 \times 10^3$, $\gamma \beta = 0.01$ and $X_0 = 0.95$. Since $\mathcal{P}_e$ is a constant independent of Ω, θ_{max}^o and q_{max}^o are constant for given constant X_0. For the calculated case $\theta_{\text{max}}^o = 5.73°$ and $q_{\text{max}}^o = 5$. However, $K_\perp^x$ is affected by B_0, so that θ_{max}^x and q_{max}^x decrease as Ω increases. If $\theta^L < \theta_{\text{max}}^x$ (dark shaded region in Figure 3), then both the o and x modes can be generated, while if $\theta^L > \theta_{\text{max}}^o$, then no EM waves are produced by LMC. For $\theta_{\text{max}}^x < \theta^L < \theta_{\text{max}}^o$ (light shaded region in Figure 3), only the o mode can be produced from Langmuir/z waves. For the above parameters, the maximum value of Ω for mode conversion to the x mode is $\Omega_{\text{max}} = 2.24$, where $q_{\text{max}}^x = 0$ and $\theta_{\text{max}}^x = 0$.

III. SIMULATIONS: PRODUCTION OF BOTH THE O AND X MODES

The sizes of each region in Figure 2's simulation box are $k_0 l_{\text{II}} = 28$ for Region II, $k_0 l_{\text{III}} = 104.5$ for Region III, and $k_0 l_{\text{IV}} = 218.5$ for Region IV. In order to describe short wavelength Langmuir/z waves as well as long wavelength EM waves, the spatial grid size dZ is chosen to be $k_0 dZ = 1/14$. The total simulation duration is from $\omega_0 t = 0$ to 4×10^4 and the time step $dt = 0.14 \omega_0^{-1}$. Initial Langmuir/z waves are generated continuously by driving the E_X and E_Z components in Region II of Figure 2 with a wave with specified frequency f and wavevector $(K_X^L, 0, K_Z^L)$. Time histories of the electric and magnetic fields in Region III are then recorded during the stationary time period, after the initial transients have died out. In the next subsections, we present the spatial dependence of the electric field and associated hodograms. The spatial dependence of the electric field shows direct evidence for LMC from Langmuir/z to EM waves, with superposition of two different outgoing EM waves for a wide range of initial conditions, and partial reflection of the incoming Langmuir/z wave. The hodograms also directly distinguish the characteristics of the outgoing EM waves. Indeed, comparing the simulation results to the theoretical ratios of the semi-major to semi-minor axes of the wave polarization for the o and x waves allows us to confirm superposition of two circularly polarized waves and to estimate the fraction of energy in each mode.

A. Spatial dependence

Figure 4 displays the electric field results for $q = 0.5$ and (a) $\Omega = 0.0$, (b) $\Omega = 0.51$, and (c) $\Omega = 2.6$. Since we inject the Langmuir/z mode with $K_Y = 0$, in the absence

of LMC there should be E_X and E_Z signals corresponding to short wavelength Langmuir/z-mode waves and no E_Y signal (since $\mathbf{K} \parallel \mathbf{E}$). However, Figure 4 shows strong evidence for LMC and production of EM waves. Specifically, E_Y is not zero for the magnetized case ($\Omega \neq 0$) and long wavelength signals exist in the E_X and E_Z components in both the unmagnetized ($\Omega = 0$) and magnetized cases.

Focusing first on the Langmuir/z-mode waves, Figure 4(a)$-$(c) shows the increased wavelength expected in Region IV as the waves propagate into the denser region. Moreover, for the magnetized cases, the polarization of the Langmuir/z mode changes near Z_{mc}, and between Z_{mc} and Z_{cut}^z the E_X and E_Y components in Figure 4(c) show longer wavelength Langmuir/z-mode waves.

Turning to the EM waves, for $\Omega = 0.51$ the EM waves in Region III show direct evidence for superposition of two modes. The evidence is that the amplitudes of the long wavelength EM waves increase in the E_X and E_Z components but decrease in the E_Y component. Since the plasma density is constant in Region III, there is no linear energy transfer between different wave modes. Thus the spatial change of the amplitudes in Figure 4(b) cannot be due to energy flow but must instead result from superposition of several waves. However, in Figure 4(a) and (c) for $\Omega = 0.0$ and 2.6, the EM amplitudes are constant in space, implying either a single EM mode or else two degenerate EM modes. In these cases the E_X and E_Z signals are a mixture of short wavelength Langmuir/z waves (incoming and reflected) plus a single EM mode. The hodograms below are consistent with two degenerate modes for $\Omega = 0.0$ and a single mode (the o mode) for $\Omega = 2.6$.

B. Hodograms

In order to investigate the characteristics of the outgoing EM waves, in Figure 5(a)-(b) we plot hodograms of the polarization of the electric field transverse to $\mathbf{B}_0$ (i.e., E_X and E_Y) for (a) $q = 0.5$ and (b) $\Omega = 0.99$, respectively. The hodograms are normalized to the maximum value in each component so that a circularly polarized field would appear as a circle. Since the long wavelength EM modes and short wavelength Langmuir/z waves have comparable amplitudes in both of E_X and E_Z, we use a wavenumber band-pass filter to extract the pure long wavelength EM waves. Figure 5(a) shows that the EM waves for $\Omega = 0.31$ are almost purely linearly polarized and that the polarization changes from linear to elliptical and then to almost circular as Ω increases: the ratios b/a of semi-major to semi-minor axes are 0.019, 0.10, 0.67, 0.37, and 0.95 for $\Omega = 0.51$, 0.71, 0.99, 1.2, and 2.6, respectively. The waves have right-handed (RH) polarization for $\Omega < 1$ and left-handed (LH) polarization for $\Omega > 1$. This polarization reversal is discussed below. We note that the magnetoionic dispersion equation shows that the o and x modes have LH and RH quasi-circular

polarizations, respectively with $b/a \approx 0.95$. Thus the EM wave for $\Omega = 2.6$ is consistent with the pure o mode, while the other cases show evidence for both the x mode and o mode.

If two circularly polarized waves are superposed, then the resulting signal can have linear or elliptical polarization. In the case of elliptical polarization, the rotation direction corresponds to the mode (RH or LH) that has higher amplitude. Accordingly the linear and RH elliptical polarizations in Figure 5(a) are strong evidence that (i) mode conversion in weakly magnetized plasmas directly produces both circularly polarized modes, (ii) the o- and x-mode amplitudes are almost the same for $\Omega \leq 0.31$, (iii) the x mode dominates for $0.5 \leq \Omega \leq 1.1$, and (iv) the o mode dominates for $\Omega > 1.2$.

In contrast to Figure 5(a), the hodograms in Figure 5(b) are all for $\Omega = 0.99$ but for different q and all show RH elliptically polarized waves. The ratio of b/a slightly decreases as q increases, with $b/a = 0.72$, 0.67, 0.62, and 0.56 for $q = 0.3$, 0.5, 0.7, and 0.9, respectively. This variation is due to changes in the fractions of o- and x-mode signals to the total field as q varies for constant Ω.

If we assume that the o and x modes are 100% circularly polarized ($|E_X| = |E_Y|$), then the relative mode amplitudes can be calculated from the normalized polarization ellipses found in the simulations: $E^{o(x)} = (a \pm b)$ for LH and $E^{o(x)} = (a \mp b)$ for RH elliptical polarizations, with $a^2 + b^2 = 1$. From the dielectric tensor, the ratio $e_{XZ} = |E_X/E_Z|$ also can be calculated for each wave mode. Thus the electric field powers are

$$E^2 = E_X^2 + E_Y^2 + e_{XZ}^2 E_X^2 \qquad (18)$$
$$= (2 + e_{XZ}^2)E_X^2. \qquad (19)$$

Then the power fractions of the o and x modes are

$$\mathcal{F}^{o(x)} = \frac{|E^{o(x)}|^2}{|E^o|^2 + |E^x|^2}, \qquad (20)$$

as plotted in Figures 5(c)-(d). For $q = 0.5$ in Figure 5(c), $\mathcal{F}^o = \mathcal{F}^x = 0.5$ in the unmagnetized limit ($\Omega = 0$). For $\Omega < 1$, as the polarizations change from linear to RH elliptical, $\mathcal{F}^x$ increases as Ω increases. This leads to $\mathcal{F}^x$ having its maximum near $\Omega = 1$. However, for $\Omega > 1$, $\mathcal{F}^x$ decreases rapidly with increasing Ω, with $\mathcal{F}^x = \mathcal{F}^o$ near $\Omega \approx 1.15$, and $\mathcal{F}^x = 0$ near $\Omega \approx 1.9$. Similarly, for a single Ω, $\mathcal{F}^x$ decreases and $\mathcal{F}^o$ increases as q increases. For example, $\mathcal{F}^x = 0.99$ for $q = 0.3$ but $\mathcal{F}^x = 0.9$ for $q = 0.90$.

The qualitative difference in o and x mode behavior for $\Omega \gtrsim 1$ requires explanation. The x mode's disappearance near $\Omega = 1$ is not a cutoff effect. Instead, as seen from Figure 3 the maximum value of Ω for which the x mode is defined for $q = 0.5$ is about 2.2, not 1.0. Section V B demonstrates that the o-mode oscillations can be explained semiquantitatively in terms of interference between the incoming and reflected Langmuir/z modes near Z_{mc}, at least for $\Omega \gtrsim 1$ where a WKB-like analysis

appears viable. Similarly, in Section V C the transmission factors along the evanescent modes connecting the Langmuir/z mode to the o and x modes are calculated and shown to explain the disappearance of the x mode above $\Omega = 1$ and the associated absence of interference effects.

IV. SIMULATIONS: MODE CONVERSION EFFICIENCIES

Calculations of the conversion efficiency ϵ require the wave power in each wave mode, obtained through a Fourier transform in Region III. In order to distinguish two different peaks in the Fourier-transformed K domain, the resolution δK should be smaller than the difference of the two wavenumbers ($\delta K \leq |K_z^1 - K_z^2|$), where $\delta K_Z = 2\pi/(l_{\mathrm{III}} k_0)$. However, for our simulations of weakly magnetized plasmas, δK_z is not sufficiently small to separate o and x modes. For instance, $|K_Z^o - K_Z^x| = 4.16 \times 10^{-2} \leq \delta K = 4.46 \times 10^{-2}$ for $\Omega = 0.99$, $q = 0.5$, and $l_{\mathrm{III}} k_0 = 104.5$. Thus the power in the o and x modes cannot be determined directly from the simulation data.

We adopt a wavenumber band-pass filter that covers both K_Z^o and K_Z^x and then average the electric and magnetic field powers according to

$$U_E(t) = \langle \widetilde{E}(K,t)\widetilde{E}^*(K,t)\rangle, \qquad (21)$$
$$U_B(t) = \langle \widetilde{B}(K,t)\widetilde{B}^*(K,t)\rangle. \qquad (22)$$

Here $\widetilde{E}_j$ and $\widetilde{B}_j$ are the bandpass-filtered Fourier transforms in space of E_j and B_j, and j represents a spatial component. Using Eqs. (19)-(20), the EM wave energy density U is

$$U = \frac{1}{2}\left(\epsilon_0 U_E + \frac{U_B}{\mu_0}\right). \qquad (23)$$

Since we analyze the time stationary period after initial transients have disappeared, this energy is constant in time.

The conversion efficiency from one mode to another can be defined using either wave energy density or wave power, both having their merits. Here ϵ is defined as the fraction of incoming Langmuir/z wave energy converted into EM wave energy:

$$\epsilon = \frac{u_{\mathrm{out}}^{EM}}{u_{\mathrm{in}}^L}. \qquad (24)$$

Alternatively, the corresponding ratio of wave powers is defined to be

$$\epsilon_s = 1 - \frac{S_{\mathrm{out}}^L}{S_{\mathrm{in}}^L} = 1 - \frac{u_{\mathrm{out}}^L}{u_{\mathrm{in}}^L} = 1 - |R^L|^2, \qquad (25)$$

where S is the Poynting energy flux and R^L is the reflection coefficient of the Langmuir/z mode. Since

$S_{\mathrm{out}}^{EM} = v_g^{EM} u_{\mathrm{out}}^{EM}$ and $S_{\mathrm{out}}^L = v_g^L u_{\mathrm{out}}^L$,

$$\epsilon = \epsilon_s \frac{v_g^L}{v_g^{EM}} \qquad (26)$$

where v_g^L and v_g^{EM} are the group speeds of the Langmuir/z and EM (o or x) modes. In general, then, ϵ and ϵ_s differ by the ratio of the group speeds v_g^L and v_g^{EM}. This ratio is a factor of order 5 in the simulations below. It is therefore quantitatively important.

Arguably it is preferable to calculate and use the conversion efficiency for wave energy densities, using Eq. (24), rather than the conversion efficiency for wave power via Eq. (25). (Of course Eq. (26) allows these two approaches to be related provided that the group speeds can be estimated adequately.) The reasons are, first, that this procedure allows separate, direct, calculation of the o- and x-mode conversion efficiencies; second, it involves directly measurable experimental quantities; and third, the "energy" conversion efficiencies are directly comparable with those predicted for nonlinear processes (e.g., Ref. [26]). In this paper, we primarily use the more general "energy" conversion efficiency of Eq. (24), but do use Eq. (25) for comparisons with previous studies. In the following subsections, the dependences of ϵ and ϵ_s on q, Ω, and polarization are presented in detail.

A. The total conversion efficiency $\epsilon(q,\Omega)$

Numerical results for the total conversion efficiency ϵ, without separation into o and x modes, are shown as a function of q and Ω in Figure 6. The parameters are $\omega_p = 2 \times 10^5$ s^{-1}, $X_0 = 0.95$, $k_0 L = 1 \times 10^3$ and $\gamma\beta = 0.01$. The results are summarized as follows, with detailed presentations deferred to the subsections below:

1. The maximum values of ϵ are less than $\approx 8\%$ for all q and Ω, with peaks of about 5% and 8% near $(q,\Omega) = (0.5,0)$ and $(0.3,1.3)$, respectively. These are smaller than the values of $50 - 70\%$ reported previously [16, 17, 19–21, 23]; however, these previous values were calculated from the power fluxes and so actually correspond to ϵ_s. Using the same definition as previous authors, with $\epsilon_s = 1 - |R^L|^2$ in Eq. (25), we recover a maximum value of ϵ_s near 50%. These values of ϵ are still much higher than the values 10^{-6} to 10^{-5} often calculated for competing nonlinear processes [26] and, since they are not averaged over the distributions of Langmuir wavevectors and gradient vectors for density irregularities, orders of magnitude higher than the 2-D and 3-D averaged efficiencies [25]. Of course, using ϵ instead of ϵ_s will reduce the 2-D and 3-D averaged efficiencies by further factors of $v_g^{EM}/v_g^L \approx 5 - 10$ from those of Ref. [25].

2. For a given q within the mode conversion window, ϵ oscillates as Ω increases. While there is also a

tendency for ϵ to decrease as Ω increases, the largest value of ϵ may occur near $\Omega = 0$ (the first peak) or at the peak of the second oscillation (near $\Omega = 1.5$ in Figure 6).

3. The values of Ω where ϵ has a local minimum ($\epsilon_{\min}$) or maximum ($\epsilon_{\max}$) decrease as q increases. For instance, $\epsilon_{\min}$ occurs at $\Omega \approx 1.8$ for $q < 0.2$ and $\Omega \approx 1.75$ for $q = 0.5$ for the situation considered.

4. The total conversion efficiency ϵ rises to a peak and then decreases as q increases, in good agreement with previous analytical studies.

5. The width $\triangle q$ in q of the mode conversion window narrows as Ω increases, with $\triangle q \propto \Omega^{-1}$. The curve $q = 2\Omega^{-1}$ is overplotted in Figure 6 and shown to provide a good approximation to $\triangle q$.

The details of ϵ as a function of q and Ω are shown in Figure 7(a) for unmagnetized and weakly magnetized cases, while Figure 7(b) shows strongly magnetized cases. Several values of Ω are chosen, marked with diamonds at the top of Figure 6. For $\Omega > 1$, these Ω correspond to the peaks $\epsilon_{\max}$ of ϵ so as to avoid the oscillation effects described in Section IV B and V B below and to allow each curve to be compared clearly.

For the unmagnetized and weakly magnetized cases in Figure 7(a), $\epsilon_{\max}$ decreases monotonically with increasing $\Omega \lesssim 1$ from values near 5.0% to 1.1% at $q \approx 0.5$. In contrast, the width $\triangle q$ of the mode conversion window is essentially constant.

For the cases $\Omega > 1$ in Figure 7(b) the peak efficiency also decreases with increasing q, although the peak efficiency at $\Omega = 1.55$ exceeds that for $\Omega = 0$. However, in addition the window narrows and shifts toward smaller value of q as Ω increases. For instance, $\epsilon_{\max}$ occurs at $q = 0.25, 0.23,$ and 0.18 for $\Omega = 1.55, 2.0,$ and 2.6, respectively. The narrowing of the window is well described by the following empirical model for the upper boundary of the window, $q = 2\Omega^{-1}$ for $\Omega > 1$, as demonstrated in Figure 6(a). For the inverse problem of incident EM waves this narrowing was predicted previously by Mjølhus [19].

Progress can also be made on predicting where the peaks $\epsilon_{\max}$ should occur. For incident EM waves (rather than the incident ES waves studied here) and $\Omega^3 \pi \gg 1$ (corresponding to $\Omega \gg 0.68$), Mjølhus [19] predicted that the maximum conversion efficiency $\epsilon_{\max}$ should occur where

$$q_M = \ln 2 \frac{2}{\pi} (k_0 L)^{-1/3} \left(\frac{Y}{1+Y}\right)^{-1/2}. \qquad (27)$$

In Figure 6 the predictions of Eq. (27) for q_M are overplotted onto the simulation results. They agree closely: from Eq. (27) $q_M = 0.29, 0.225,$ and 0.175 for $\Omega = 1.5, 2.0,$ and 2.6, while the simulations yield $q_M = 0.27, 0.25,$ and 0.18 for $\Omega = 1.55, 2.0$ and 2.6, respectively.

In summary, the foregoing results demonstrate in detail that including the magnetic field ($\Omega > 0$) leads to large oscillations in ϵ, with an overall decreasing trend, as Ω increases (expanding on Ref. [4]). In addition, the results agree with previous studies that the width $\triangle q$ narrows as Ω increases [16, 19], obeying $\triangle q \approx 2q^{-1}$, and that the peaks of ϵ with q agree well with the prediction of Eq. (27) for the inverse problem [19].

B. Conversion efficiencies for the o and x modes

Combining the fractions $\mathcal{F}^o$ and $\mathcal{F}^x$ of o- and x-mode power to the total power in Figure 5(b) with the total efficiencies from Figure 6, we can calculate the separate conversion efficiencies from the Langmuir/z mode to the o and x modes, ϵ^o and ϵ^x, as functions of q and Ω. Rather than two such contour plots, Figure 8(a) shows ϵ^o and ϵ^x as functions of Ω for $q = 0.5$. It is evident that ϵ and ϵ^o decrease and oscillate as Ω increases while ϵ^x decreases monotonically. Put another way, the o- and x-mode conversion efficiencies vary in qualitatively different ways for $\Omega \gtrsim 1$, with the o mode dominating and determining the total conversion efficiency for $\Omega \gtrsim 1$ (for $q = 0.5$). However, for $\Omega \lesssim 1$, the o- and x-mode efficiencies are very similar in magnitude and vary in almost identical ways as Ω increases.

Oscillations of ϵ in Ω are explained in terms of interference effects between incoming and reflected Langmuir/z waves in Section V B. Here we point out only that Figure 8(b) displays the relative phase ϕ predicted as a function of Ω and that the interpretation is convincing for $\Omega \gtrsim 1$: except for the first maximum centered near $\Omega = 0$, the maxima and minima in ϵ^o are located near $\phi \approx 2n\pi$ and $(2n+1)\pi$ (for integer n), respectively.

Mjølhus [19] predicted that the maximum conversion efficiency in a magnetized plasma would be one half of the unmagnetized result. This is incorrect, based on Figures 6 and 7, if one considers the total conversion efficiency to EM waves. However, it is clear that in the unmagnetized and weakly magnetized limits (e.g., $\Omega \lesssim 0.5$) approximately half the radiation comes out in each of the o and x modes, so that Mjølhus's statement is correct for each EM mode separately.

A crucial aspect of Figures 5 and 8(a), examined in detail in Section V below, is that small variations in Ω about unity can lead to substantial variations in the net polarization of the resulting waves. Specifically, the net polarization can range from near zero to strongly LH to strongly RH circular polarization.

C. Comparison of the power conversion efficiencies ϵ_s vs. q with previous work

This subsection compares the simulation results for the power conversion efficiency ϵ_s with previous unmagnetized and magnetized studies for various X_0. Previous work includes numerical simulations of the unmagnetized fluid equations for LMC of incident EM waves in a warm

plasma [17], numerical solutions of the wave equations for Langmuir waves with $X_0 = 0$ or $X_0 = 0.5$ incident on warm unmagnetized [21, 23] or warm magnetized [16] plasmas, and an analytical solution for incident EM waves in cold unmagnetized plasma [22]. Figures 9 and 10 compare the simulations with the previous unmagnetized and magnetized results, respectively.

Figures 9(a) - (b) demonstrate impressive agreement between the simulations and analytic results for $X_0 = 0.95$. They also show very good agreement between the simulations and previous numerical solutions (differences of only $1 - 10\%$ at $q = 0.5$). Note firstly that the maximum values of ϵ_s are $\approx 50\%$, obtained at $q = 0.5$. Second, although we assumed larger values of $\gamma\beta = 0.01$ than Refs [17] and [21] ($\beta = 0.005$ and 10^{-5}, respectively), the excellent agreement shows that the effect of β on ϵ is very small, consistent with statements in Refs [17] and [25].

Ref. [21] predicts that the maximum in ϵ_s increases and the range of q with nonzero ϵ_s decreases as X_0 approaches unity. Figure 9(c) shows these trends. In contrast to the results for $X_0 = 0.95$, when $X_0 = 0.985$ the maximum of ϵ_s is $\sim 56\%$ at $q = 0.4$, mode conversion only occurs for $q \leq q^o = 1.5$ ($q^o = 5$ for $X_0 = 0.95$), and the simulation results show the ϵ_s is zero at $q = 1.5$. The simulation results are compared with Ref. [21]'s results for $X_0 = 0.5$ and 0.995, finding excellent agreement with the result for $X_0 = 0.5$ and the same trends as the result for $X_0 = 0.995$. The decrease in the mode conversion window with increasing X_0 comes from the dependence $q_{max} \propto (1 - X)$ in Eqs (14) and (15) [21]. The very good agreement with our simulations confirms the prediction [21] that the dependence on X_0 is very important for Langmuir/z waves under solar wind conditions (because $X_0 \approx 1.0$ there).

Figure 10 compares the simulation results with approximate numerical solutions of the wave equations for $\Omega = 0.99$ [16]. Since ϵ is expected to be a function of Ω rather than $k_0 L$ or Y alone, the two sets of results have the same Ω but different $k_0 L$ and Y: $k_0 L = 1 \times 10^3$ and $Y = 9.75 \times 10^{-3}$ for our simulations and $k_0 L = 192$ and $Y = 0.03$ for Ref. [16]. The two sets of results do not agree well, differing by a factor ≈ 5 in ϵ_s and with different locations for the peak ($q = 0.5$ for the simulations but 0.38 in Ref. [16]).

It is believed that the simulation results in Figure 10 are correct. The reasons are the very good agreement between the simulation results and previous unmagnetized results, the lack of approximations made in the simulation model, and the agreement of the simulation results with new analytic theory (see Sections V.A - V.C below). We speculate that the differences in Figure 10 between the results of Ref. [16] and the simulations are due to the approximations made in Ref. [16], which also led to the neglect of interference effects between the incoming and outgoing Langmuir/z waves. It is relevant that the o-mode efficiency varies strongly and interference effects are large near $\Omega = 1.0$, as seen in Figures 5, 6, and 8 and discussed in depth in Section V.B below.

Finally, based on Figure 6 we note that for weakly magnetized plasmas the mode conversion window $\triangle q$ does not narrow significantly with increasing Ω, until $\Omega \gtrsim 1$. Moreover, Figure 6 shows that the simulations predict values of q for the peaks in ϵ and ϵ_s that agree well with previous results for strongly magnetized plasmas [19].

V.   ANALYSIS

This Section explores the evanescent modes connecting the Langmuir/z, o, and x modes and develops a WKB-like theory for interference of the Langmuir/z modes near Z_{mc}, associated oscillations in the conversion efficiency for the o mode, transmission factors for energy flows along the evanescent modes, and the associated implications for the conversion efficiencies into the o and x modes. In addition, the net polarization of the output radiation is calculated and constraints placed on the levels of density fluctuations if the x mode is to be generated and propagate.

A.   Dispersion Relations

The coupling of Langmuir/z mode waves into EM waves in an inhomogeneous plasma occurs due energy tunneling into evanescent modes that connect propagating modes in frequency - wavevector and physical space. These evanescent modes are related to cutoffs (where the refractive index of a propagating mode goes to zero) and occur in so-called stop bands in $\omega - \mathbf{k}$ space and stop zones in physical space. Here the propagating modes are the Langmuir/z, o, and x modes, all of which have distinct cutoffs in a magnetized plasma.

The refractive index curves for the Langmuir/z, o, x, and connecting evanescent modes are illustrated in Figure 11 as functions of wavenumber $K_\parallel$ and frequency X for $K_\perp = 0.07$, $\omega_p/\omega_c = 100$, and $\gamma\beta = 3 \times 10^{-4}$. Viewing the wave properties as a function of $X_e = f_p^2/f^2$, it is found that evanescent modes appear in association with the three stop bands that exist at larger X_e than the x, o, and z mode cutoffs. The Langmuir/z, o, and x modes have cutoffs at X_{cut}^z, X_{cut}^x, and X_{cut}^o, respectively, with

$$X_{cut}^o = 1 - K_X^2, \qquad (28)$$

$$X_{cut}^x = \frac{c_1 - \sqrt{c_1^2 - 4c_2}}{2}, \qquad (29)$$

$$X_{cut}^z = \frac{c_1 + \sqrt{c_1^2 - 4c_2}}{2}, \qquad (30)$$

$$c_1 = 2 - K_X^2, \qquad (31)$$

$$c_2 = (1 - Y^2)(1 - K_X^2). \qquad (32)$$

In comparison, the nominal mode conversion point occurs where

$$X_{mc}^o = 1. \qquad (33)$$

The Langmuir/z, o, and x modes are clearly visible in Figure 11 as real solutions that exist where X_e exceeds X_{cut}^z, X_{cut}^o and X_{cut}^x, respectively. An imaginary solution named the x' mode connects the x mode to the o mode between X_{cut}^x and X_{cut}^o. This x' solution is purely imaginary, corresponding to an evanescent mode. A complex o'' mode connects the o mode to the z mode, while an evanescent o' mode exists above X_{cut}^o and an evanescent z' mode exists above the z-mode cutoff. Thus near X_{cut}^o the dispersion curves for the o, o'', and x' modes join each other, while the o'' and z-modes encounter each other near X_{mc}. This means that energy in the Langmuir/z mode propagating from higher density regions to Z_{mc}, for instance via reflection at the z cutoff of Langmuir/z waves propagating towards higher density regions, can reach X_{cut}^o through the o'' branch and then partially flow into the o and x' branches. Accordingly, some wave energy reaching X_{cut}^o might tunnel along the x' mode and thence reach X_{cut}^x, where it can appear as x-mode radiation. Note that the imaginary part of the x' solution is typically smaller than that of the o'' mode, suggesting that the conversion efficiencies into the o and x modes may be primarily determined by coupling from the z into the o'' mode and so be rather similar in magnitude. This is rather unexpected according to previous work, but is consistent with the simulation results, as shown in Section V C.

In addition, another mechanism potentially exists: some energy might couple into the o'' mode via the resonance at Z_{mc}, where the Langmuir/z mode becomes linearly polarized and changes its sense of circular polarization (righthand at smaller X_e and lefthand at larger X_e), and eventually reach the o and x modes via the evanescent modes above. This mechanism relates to Langmuir/z waves propagating both into and out of the density inhomogeneity. The good agreement shown below between the WKB-like theory and simulations suggests that this mechanism does not occur in practice.

B. Interference Effects

In a magnetized plasma, unlike the unmagnetized case, Langmuir/z waves can propagate through the Z_{mc} region twice: as illustrated in Figure 1, once when propagating into the density gradient and once after reflection at the z cutoff. Assuming that a WKB style analysis is appropriate (meaning that the wavelength is small compared with the scale lengths for the density gradient), the phase difference ϕ at Z_{mc} between the incoming and reflected Langmuir/z modes is then

$$\phi = \pi + 2\int_{Z_{\mathrm{mc}}}^{Z_{\mathrm{cut}}^z} dZ' \; K_Z^L = \pi + 2\int_{z_{\mathrm{mc}}}^{z_{\mathrm{cut}}^z} dz' \; k_z^L \quad (34)$$

where the first and second forms of the equation's right hand side are written for normalized and physical variables, respectively. Here $Z' = k_0 z'$ denotes distance

along the wave path from $Z_{\mathrm{mc}} = k_0 z_{\mathrm{mc}}$ and $Z_{\mathrm{cut}}^z = k_0 z_{\mathrm{cut}}^z$. The constant term π comes from assuming a change in phase of π at the reflection point Z_{cut}^z. The quantity $K_Z = k_z/k_0$ is the normalized component of the (real part of the) wavenumber k_z parallel to $\mathbf{B}_0$ of the Langmuir/z mode as a function of Z.

For a 1-D linear density gradient, the two points Z_{mc} and Z_{cut}^z are separated by a distance

$$\triangle Z = |Z_{\mathrm{mc}} - Z_{\mathrm{cut}}^z| = \left(1 - \frac{X_{\mathrm{mc}}}{X_{\mathrm{cut}}^z}\right) k_0 L \approx Y k_0 L. \quad (35)$$

The final form of Eq. (35) follows from Eqs (30)-(32) in the limit $K_X^2 \ll 1$. Proceeding from this limit and using Eq. (10), Eq. (35) may then be rewritten as

$$\triangle Z = \Omega^2 (k_0 L)^{1/3} \; . \quad (36)$$

Figure 12 plots $\triangle Z$ as a function of $k_0 L$ and K_X for $\Omega = 1.5$. The solid curve's prediction of Eq. (36) agrees increasingly well with the numerical predictions for $\triangle Z$ as $q = (k_0 L)^{2/3} K_X^2$ decreases from the value 0.5 to 0.1. This is consistent with Eq. (36) applying in the limit $K_X^2 \ll 1$.

The strong dependence of the phase difference ϕ in Eq. (34) on $\triangle Z$ thus implies that ϕ and so ϵ_s should also vary with $k_0 L$, Ω (and so Y), and K_X. Specifically, in the limit $K_X \ll 1$ Eqs (34) and (36) result in the prediction

$$\phi \approx \pi + 2\Omega^2 (k_0 L)^{1/3} \langle K_Z^L \rangle \; , \quad (37)$$

where $\langle K_Z^L \rangle$ is the average value of K_Z^L over the propagation path. Qualitatively, then, Eq. (37) predicts that ϕ should depend on Ω, $k_0 L$, K_X, and $\langle K_Z^L \rangle$. This equation and its more general form Eq. (34) thus have the potential to explain the dependence on Ω and q of the interference effects in Figure 8.

If $\phi \to (2n+1)\pi$ for integer n, then the wave amplitude at Z_{mc} should have a minimum value due to destructive interference. Figure 8(b) shows the prediction of Eq. (34) for ϕ as a function of Ω for $X_0 = 0.95$, $\omega_{p0} = 2 \times 10^5 \text{ s}^{-1}$, $k_0 L = 1 \times 10^3$, and $\gamma\beta = 0.01$. Here the required values of K_Z^L are calculated numerically for a specified q from the dispersion equation for a spatially uniform but warm Maxwellian plasma. Clearly the values of Ω corresponding to $\phi \approx (2n + 1)\pi$ correlate well with minima in ϵ^o in Figure 8(a), and so in Figure 6. Similarly $\phi \approx 2n\pi$ very near values of Ω where maxima in ϵ^o occur, except for the first maxima centered near $\Omega = 0$.

Now consider the analytic prediction of Eq. (37) in connection with Figure 8. Choosing $\Omega = 1.5$ and $k_0 L = 10^3$ yields $\phi = \pi + 30\langle K_Z^L \rangle$. Inspection of Figure 11 suggests that the value $\langle K_Z^L \rangle \approx 0.1$ is reasonable, so that $\phi \approx 2\pi$ and constructive interference can be expected. For $\omega = 1.7$ Eqn (37), close to where a minimum is found, then predicts $\phi \approx 2.8\pi$, so being close to destructive interference. The approximate analysis of Eqs (34)-(37) thus provides a good quantitative explanation for the observed oscillations. Thus, these aspects of

Figure 8 and Eqs (34)-(37) provide strong evidence that interference between incoming and outgoing Langmuir/z waves leads to the oscillations observed for $\Omega \gtrsim 1$ in the conversion efficiency of the o mode.

According to Figure 8(b) then, the polarization reversal near $\Omega = 1$ in Figure 5 is not due to large ϵ^x. Instead this is primarily due to ϵ^o decreasing via interference and, to a lesser extent, to numerical errors in separating ϵ^0 and ϵ^x.

Since $\phi = \phi(K_Z, \triangle Z)$ via Eqs (32)-(33), ϕ is also a function of q as well as Ω. This offers the potential of explaining Figure 6's oscillations in Ω and the associated changes in q. Accordingly Figure 13(a) plots the values of q as a function of Ω where $\phi = \pi$ and 2π. Clearly the curves move to slightly smaller q as Ω increases. Put another way, for sufficiently strongly magnetized plasma, interference effects cause the maxima and minima in ϵ^o to vary with q as well as Ω. Thus the net polarization of the outgoing EM waves varies with q for a single Ω. However, variations of ϵ^o for a single Ω are greater than for a single q. Figure 13(b) superposes the predicted pattern of minima for ϵ onto Figure 6's simulation results. The agreement is qualitatively convincing and reasonable quantitatively, though for $\Omega < 2.2$ the simulation results are shifted to lower Ω than the predicted pattern.

Thus it appears that interference effects can explain many aspects of the oscillations drifting to lower q with Ω in the efficiency of mode conversion. Put another way, the foregoing phase analysis, 8, and Figure 13 quantify and strongly justify the idea that interference between Langmuir/z waves is important for LMC. Indeed, this analysis quantitatively justifies for the first time, albeit via the inverse process of LMC of Langmuir/z waves into o-mode waves, an earlier suggestion by Mjøhus [20] that interference effects might be important in LMC of o-mode waves into Langmuir/z waves. However, several questions remain. First, why does the interference prediction break down for $\Omega \leq 1$, where it clearly misses the maximum centered near $\Omega = 0$ and wrongly predicts destructive interference and small ϵ? Second, why do these interference effects appear in ϵ^o only, and apparently not in ϵ^x? Third, does ϕ depend on $k_0 L$ as well as on Ω and Y?

Regarding the first question, note that the WKB approach requires that the wavelength be small compared with spatial scales of interest. However, Figure 4 shows that the spatial size of the region between the o-mode cutoff and mode conversion point, $\triangle Z$ given by Eq. (35), is small compared with the wavelength of the Langmuir/z-mode wavelength in the density irregularity until $\Omega \gtrsim 1$. This shows that the WKB analysis is not well justified for $\Omega \lesssim 1$, suggesting that the WKB approach breaks down and the prediction (34) becomes inaccurate. Put another way, where $\Omega \geq 1$ the WKB approach is justifiable, Eq. (34) should apply, and the oscillations in ϵ^o are well explained in terms of interference of incoming and outgoing Langmuir/z waves.

Second, the x mode is allowed for $\Omega \leq 2.2$ accord-

ing to Figure 3. If the x mode is formed by tunneling into the x' mode, with energy entering both the o and x' modes from the o' mode, itself fed energy near Z_{mc} where the z mode experiences interference effects, then the simplest expectation is that the x mode should show interference effects if the o mode does and $\Omega \leq 2.2$. That is, the x mode should show interference effects where Eq. (35) applies, meaning $1 \lesssim \Omega \lesssim 2.2$. However, analysis of transmission factors in the next subsection provides a quantitative explanation for the lack of interference effects experienced by the x mode while also explaining why the o mode does experience them.

C. Transmission factors and polarizations

LMC and the coupling between modes may be treated semiquantitatively by noting that the waves decay spatially in regions where $K_\parallel$ is complex. This spatial decay can be described in terms of an transmission factor $\mathcal{A}$ for the wave energy [2, 28], with

$$\mathcal{A} = \exp\left(-\int_{Z_1}^{Z_2} dZ' \, |\text{Im} K_\parallel| \right). \tag{38}$$

where Z' denotes a spatial distance along the wavepath from Z_1 and Z_2 parallel to $\mathbf{B}_0$. This distance is related to the cutoffs in X by equations analogous to Eq. (35). Note that $A = 1$ in the limits $K_\parallel \to 0$ and $Z_1 \to Z_2$, corresponding to perfect transmission and zero attenuation.

Numerical results for the transmission factors $\mathcal{A}^{mo}(q, \Omega)$ between Z_{mc} and Z_{cut}^o, $\mathcal{A}^{ox}(q, \Omega)$ between Z_{cut}^o and Z_{cut}^x, and $\mathcal{A}^{mx}(q, \Omega) = \mathcal{A}^{mo}\mathcal{A}^{ox}$ between Z_{mc} and Z_{cut}^o are shown as contour plots in Figure 14 using Table 1's parameters. These are the transmission factors for the o'', x', and combined $o'' - x'$ couplings. The conversion from the o'' to the o mode corresponds to $\mathcal{A}^{mo}$ while the conversion from o'' to x corresponds to $\mathcal{A}^{mx}$. Figure 14s calculations use the typical parameters in Table I for ω_p, ω_p/ω_c and $\langle L \rangle$ in the solar wind at 1 AU and in the corona.

In Figures 14(a)−(b) $\mathcal{A}^{mo}$ decreases monotonically as q and Ω increase, but is primarily affected by q rather than Ω: $\mathcal{A}^{mo}$ is almost zero for $q \geq 1.4$. This factor explains qualitatively why the conversion efficiencies decrease with q for large enough q in Figures 6–7, 9–10. Indeed, the large decrease in $\mathcal{A}^{mo}$ to almost zero for $q \gtrsim 1.4$ accounts semiquantitatively for the width $\triangle q$ of the conversion window in q. Moreover, the slow decrease in $\mathcal{A}^{mo}$ with increasing Ω at moderate q is qualitatively consistent with $\triangle q$ decreasing as Ω increases in Figures 6 and 13. Finally, the variations of $\mathcal{A}^{mo}$ and $\mathcal{A}^{mx}$ with q do not explain the peak in conversion efficiency occurring at intermediate $q \approx 0.2 - 0.5$ in the above Figures.

Figures 14 (c)−(d) show that $\mathcal{A}^{ox}$ decreases monotonically with increasing Ω at constant q, with a very sudden and dramatic decrease near $\Omega \approx 1$, while it increases slowly with increasing q at constant Ω. Since

$\mathcal{A}^{mx} = \mathcal{A}^{mo}\mathcal{A}^{ox}$, Figures 14 (e)−(f) show that $\mathcal{A}^{mx}$ decreases rapidly with both q and Ω, being closely similar in magnitude to $\mathcal{A}^{mo}$ only for $\Omega \lesssim 1$ and significantly greater than zero only for $\Omega \lesssim 1.5$ and $q \lesssim 1.4$.

The very similar magnitudes of $\mathcal{A}^{mo}$ and $\mathcal{A}^{mx}$ for $\Omega \lesssim 1$ provide a direct semiquantitative explanation for, first, why the x mode is produced under these conditions (the evanescent damping is essentially all along the o'' mode and not along the x' mode) and, second, why the o- and x-mode conversion efficiencies are essentially identical, provided only that $\nu \approx 0.5$. This first point and the associated finding of small damping along the x' mode for $\Omega \lesssim 1$ directly contradict the reasonable (but incorrect) assumption of large evanescent damping of the x'-mode by previous workers, which led to their prediction that LMC would produce only the o mode. Furthermore, the sudden and large decrease in $\mathcal{A}^{mx}$ near $\Omega = 1$ provides a direct semiquantitative explanation for why no interference effects (and associated oscillations in ϵ^x with increasing Ω) are found for $\Omega \gtrsim 1$. This behavior also explains why $\epsilon^x \approx 0$ for $\Omega \gtrsim 1.5$ despite the x mode existing for $\Omega \lesssim 2.2$ (see Figure 3).

One final issue relating to Figure 14 is that Figure 6's results show the peak conversion efficiencies occurring at intermediate $q \approx 0.2 - 0.6$ (depending on Ω), and not near $q = 0$ as predicted in Figure 14. One possible explanation, based on Eqs (39)–(41) is that the factor $\mu(q, \Omega)$ peaks at intermediate q. This is necessarily true since zero LMC occurs for $q = 0$, because the connecting modes do not exist [3], but needs to be quantified. Another possible problem is that, once again, the WKB-style analysis of Eq. (34) breaks down for small Ω. Further work is thus required to explain why the peak values of ϵ occur at intermediate values of q.

D. Polarizations

In principle the foregoing results based on Eq. (34) allow the net polarization of the radiation to be predicted analytically. Specifically, the ratios $r^o(q, \Omega)$ and $r^x(q, \Omega)$ of the wave energy reaching the o and x mode, respectively, to the total Langmuir/z-mode energy at $X^o_{\rm cut}$ are

$$r^o(q, \Omega) = \mu(q, \Omega)\nu(q, \Omega)\left[\mathcal{A}^{mo}(q, \Omega)\right]^2 , \quad (39)$$

and

$$r^x(q, \Omega) = \mu\left[\mathcal{A}^{mo}\right]^2(1 - \nu)\left(\mathcal{A}^{ox}\right)^2 \quad (40)$$

$$= \mu(q, \Omega)\left[\mathcal{A}^{mx}\right]^2 - r^o(q, \Omega)\left[\mathcal{A}^{ox}\right]^2 . \quad (41)$$

Here $\mu(q, \Omega)$ is the ratio of Langmuir/z-mode energy at $X_{\rm mc}$ to that entering the o'' mode while $\nu(q, \Omega)$ is the fraction of o'' mode energy reaching the o-mode cutoff that enters the o mode. Note that the $(1-\nu)$ term in Eq. (36) assumes that all o'' energy reaching $X^0_{\rm cut}$ goes into either the o or x' modes. Furthermore, based on $r^x \approx r^0$ for $\Omega \lesssim 0.5$ in Figures 5 and 8, we expect $\nu \approx 0.5$.

The net degree of polarization of the emitted radiation can then be calculated using the predictions r^o and r^x of Eqs (39)–(41) and an assumption for ν, or directly from the simulations, using

$$P = \frac{r_o - r_x}{r_o + r_x} \quad (42)$$

$$= \frac{\nu - (1 - \nu)[\mathcal{A}^{ox}]^2}{\nu + (1 - \nu)[\mathcal{A}^{ox}]^2}. \quad (43)$$

For $r_o = r_x$, $P = 0$, and the waves have linear polarization. On the other hand, when $r_x = 0$, $P = 1$ and the waves have LH polarization while if $r_o = 0$ then $P = -1$ and the waves have RH polarization. More generally, it is clear from Eqs (35)-(36) that P should be independent of μ but that the ν terms do not cancel out in general.

Before proceeding, note that in principle the interference effect in Section V B could be included via a factor $|1 + e^{i\phi}|^2$, with ϕ given by Eq. (34). This is not done here so that the regime $\Omega \lesssim 1$, where the WKB analysis is not well justified and the factor is close to zero, can be investigated.

E. Effects of Density fluctuations

LMC between the Langmuir/z and x modes requires two conditions: (1) the wave frequency must exceed the x mode's cutoff frequency and (2) the wave energy that tunnels to the x-mode cutoff is nonzero. The second condition is already considered above. The first condition $f > f^x_{\rm cut}$ is satisfied when $X_e < X^x_{\rm cut}$. Since $X_e \propto \omega_p^2 \propto N_0$, the condition on X_e becomes a constraint on N_0 and the maximum level of density fluctuations δN_0 for the x mode to be able to propagate.

Figure 15(a) illustrates the relationship between δN_0 and X_e. Consider a Langmuir wave with frequency f_0 that is generated at a local maximum in the density (point $Z_{\rm max}$) that propagates toward the mode conversion region through the point $Z_{\rm min}$ which has minimum density. At point $Z_{\rm min}$, if $f_0 > f^x_{\rm cut}$, then Langmuir/z energy can mode-convert into the x mode. Thus the condition $f_0 = f^x_{\rm cut}$ provides the condition for x-mode propagation. In this case, the change in density δN between points $Z_{\rm max}$ and $Z_{\rm min}$ is given by

$$\delta \widetilde{N}_{\rm min} = \frac{N_0 - {\rm Min}\left[N(z)\right]}{N_0} \quad (44)$$

$$= \frac{f_{p0}^2 - (f^x_{\rm cut})^2}{f_{p0}^2} \quad (45)$$

$$= 1 - (X^x_{\rm cut})^2, \quad (46)$$

with

$$(X^x_{\rm cut})^2 - [2 + r_{pc}^{-2} + (1 + r_{pc}^{-2})K_X^2]X^x_{\rm cut}$$
$$+ 1 - K_X^2 = 0, \quad (47)$$

$$r_{pc} = \omega_p/\omega_c. \quad (48)$$

Thus if we know K_X and r_{pc}, then δN can be estimated easily.

Figures 15(b)–(c) show the situations $\delta \widetilde{N}_0 > \delta \widetilde{N}_{\min}$ and $\delta \widetilde{N}_0 < \delta \widetilde{N}_{\min}$, respectively, where $\delta \widetilde{N}_0 = \triangle \widetilde{N}_0 / N_0$. If $\delta \widetilde{N} > \delta \widetilde{N}_{\min}$ as in Figure 15(b), then the x mode can be produced by LMC and propagate. However, if $\delta \widetilde{N} < \delta \widetilde{N}_{\min}$ then only the o mode can be produced by LMC and propagate in free space.

VI. APPLICATIONS

LMC is a possible mechanism for the electromagnetic radiation produced just above f_p, in type II and III radio bursts in the corona and solar wind as well as radiation from Earth's foreshock. (The $2f_p$ components of these emissions cannot be produced by the LMC process considered here, although other linear conversion mechanisms are possible.) Now consider the implications of Sections II to IV for these f_p radiations.

The nominal values of Ω in the solar wind and corona are $\Omega_{sw} = 0.87$ and $\Omega_{co} = 0.98$, respectively, based on the parameters in Table I. These values are shown in Figures 14(c)−(f) as dotted lines. For $q \leq 1$ $\mathcal{A}^{mo} \geq 0.4$ and $\mathcal{A}^{mx} \geq 0.4$ for the solar wind while and $\mathcal{A}^{mo} \geq 0.3$ and $\mathcal{A}^{mx} \geq 0.3$ for the corona. In both cases, the calculations imply that Langmuir/z-mode energy can tunnel effectively into both the o and x modes. Similarly, Figures 5, 6, 8, and 13 suggest that both o- and x-mode radiation should be produced for values of Ω, q, and k_0L similar to those for the nominal coronal and solar wind parameters in Table 1.

The foregoing calculations were for $\gamma\beta = 0.01$, which corresponds to unrealistically high temperatures for the corona and solar wind. Figure 16 therefore examines the effects of temperature on the transmission factors $\mathcal{A}^{mo}$, $\mathcal{A}^{ox}$, and $\mathcal{A}^{mx}$ calculated from Eq. (34) for the solar wind at 1 AU ($\Omega_{sw} = 0.87$) and the corona ($\Omega_{co} = 0.98$). We use $\gamma\beta = 0.0001$ and 0.25 for the solar wind and $\gamma\beta = 0.01$ and 0.25 for the corona. As expected from Figure 14, in Figure 16 $\mathcal{A}^{mo}$ and $\mathcal{A}^{mx}$ decrease while $\mathcal{A}^{ox}$ increases with increasing q. The Figure shows that the temperature effects on A^{mo} are very small (changing by less than a few percent) while $\mathcal{A}^{ox}$, and $\mathcal{A}^{mx}$ change very little (at most 10%) with different $\gamma\beta$. Finding that the effects on $\mathcal{A}^{mo}$ and $\mathcal{A}^{mx}$ of varying $\gamma\beta$ is very small can be understood by noting that $\text{Im}(K) \gg v_{th}k_0$, so that thermal terms are small. Thus the energy ratio μ at Z_{cut}^o in (39) is almost the same for different β. This result is consistent with the work of Refs [17] and [21], which showed that the mode conversion efficiency changes very little with thermal speed. Similarly, comparisons of the simulation results and previous analytical results in Figure 9 with the simulation results in Figure 6 and analytic results of Figures 14 and 16 are all consistent with the effects of β being very weak.

Thus, based on these calculations, LMC can be ex-

pected to produce both o and x-mode radiation for type II and III bursts in the solar wind near 1 AU and in the corona, as well as for radiation from Earth's foreshock. Previous predictions that LMC should produce only o-mode radiation in these contexts appear to be incorrect.

The prediction that LMC can produce both o- and x-mode radiation for type II and III bursts is relevant to the relatively low degree of circular polarization observed. Rather than the 100% o-mode polarization expected traditionally [28], type IIs are almost always less than 10% polarized, whereas type IIIs are typically less than 30% polarized and always less than 70% [27]. Figures 5, 8, 14, and 16 suggest a natural resolution to this "depolarization problem" provided that LMC is relevant: (i) almost equal amounts of o and x mode are produced for $\Omega \lesssim 0.4$, yielding radiation with almost zero net circular polarization, and (ii) when $0.4 \lesssim \Omega \lesssim 1.3$ the radiation has a relatively small net polarization that can be net righthand or lefthand depending on Ω and q. Only when $\Omega \gtrsim 1.6$ is pure o-mode radiation expected from LMC.

Figures 8 and 13 also suggest that the relative fraction of o- and x-mode radiation is sensitively dependent on the density turbulence and plasma magnetization near $\Omega \approx 1$, just near Table 1's nominal values for the corona and solar wind near 1 AU. Specifically, Figure 8 predicts that the x mode polarization should be dominant for $0.4 \lesssim \Omega \lesssim 1.1$, with the o mode dominant for higher Ω. Thus the sense of net circular polarization, if it can be established to definitely be in the sense of the o mode versus the x mode (which requires knowledge of the coronal magnetic field direction), might provide a sensitive observational constraint on Ω.

The primary reasons for the net polarization depending sensitively on Ω near $\Omega = 1$ are the monotonic decrease in the x-mode conversion efficiency and the interference effect for the o mode. Section V.D's analytic formalism can be employed to assess these two effects. Since the net degree of polarization P is a function of ν and $\mathcal{A}^{ox} = \mathcal{A}^{ox}(q)$ in Eq. (43), for a single Ω P can be predicted as a function of q and ν using Eqs (38) and (43).

Figure 17 therefore compares P as a function of q and ν for $\Omega_{sw} = 0.87$ (solar wind) and $\Omega_{co} = 0.98$ (corona), respectively. Figure 17(a) shows clearly that P changes very little with q for a single ν: P decreases as q increases, but the differences in P for $q = 0.1$ and $q = 1.5$ are only 20% for $\nu = 0.2$ and $\nu = 0.8$. Moreover, just as found for the transmission factor $\mathcal{A}$ in Figure 17, thermal effects on the degree of polarization are very weak. However, Figure 17(b) predicts that P increases rapidly from negative to positive values (changing from net x-mode to net o-mode polarization) as ν increases from 0 to 1. For instance, $P = -46\%$ at $(q, \nu) = (0.5, 0.2)$ and $P = +71\%$ at $(q, \nu) = (0.5, 0.8)$.

The quantity ν is constrained by the simulations: since they yield equal amounts of o and x radiation for small Ω, it is most likely that $\nu = 0.5$. (However, ν could in principle be a function of Ω and/or other parameters.) Thus for $\nu = 0.5$ Figure 17 predicts that $P(q)$ ranges

from +5 to +41% and +10 to +58% for various q and the nominal solar wind and coronal parameters, respectively. However, these senses of polarization (positive corresponds to o mode being dominant) are inconsistent with Figures 5 and 8. This inconsistency is believed due to neglect of interference effects and the breakdown of Eq. (38)'s WKB analysis for $\Omega \lesssim 1$. Future developments should be directed at removing these limitations of the present theory.

Finally, consider the constraints of Section V.D as to whether the x mode can plausibly propagate from source regions in the corona and solar wind. The quantities X_{cut}^x and $\delta\widetilde{N}$ are calculated using Eq. (47) and plotted in Figure 18. Values $\gamma\beta = 10^{-4}$ and 10^{-2} are assumed for the solar wind at 1 AU and the corona, respectively. In Figure 18 X_{cut}^x decreases as q increases and the maximum values of X_{cut}^x are 0.99 and 0.90 for the solar wind and corona at $q = 0$, respectively. When $X_e < X_{cut}^x$ the x mode can propagate. Using Eq. (46), $\delta\widetilde{N}_{min}$ can be calculated from X_{cut}^x and is 1% and 10% for the solar wind and corona at $q = 0$, respectively. Thus, if $\delta\widetilde{N}_0 \geq$ 1% in the solar wind and $\delta\widetilde{N}_0 \geq 10\%$ in the corona, then Langmuir/z waves will have frequencies that exceed f_{cut}^x and the x mode will be able to propagate out of the mode conversion region.

Celnikier et al. [35] present data from the ISEE-1 and -2 spacecraft that show $\delta\widetilde{N}_0$ to be $2 - 10\%$ in the solar wind. Moreover, the relative level of $\widetilde{N}_0$ near 1 AU is often believed to be independent of heliocentric distance interior to 1 AU [36]. Thus, our calculations of the minimum levels of $\widetilde{N}_0$ in the solar wind and the corona are not inconsistent with previous observational and theoretical results. This implies that the x-mode can exist near and propagate from mode conversion regions in the solar wind and corona. Thus, it appears as though the simulations, theoretical constraints, and available observational data all imply that LMC in the source regions of coronal and interplanetary type II and III bursts, and in Earth's foreshock, should result in both o- and x-mode radiation.

VII. DISCUSSION AND CONCLUSION

We have presented numerical simulations of LMC from Langmuir/z to EM waves and analytical calculations of mode coupling in warm magnetized plasmas. The simulation results show strong evidence that high levels of x- and o-mode radiation can be produced from Langmuir/z wave via LMC, with the relative fraction of energy in the x and o modes varying with the parameter Ω. They are supported by new numerical calculations which predict that significant amounts of Langmuir/z wave energy should tunnel into both the x and o modes from the nominal mode conversion point Z_{mc}. Moreover, it is shown that the Langmuir/z-mode waves can have frequencies above x-mode cutoff frequency f_{cut}^x and that the x-mode radiation can propagate to the lower density side and

outside the source region if specific constraints on the level of density turbulence are met. It is found that the constraints on the density turbulence are not inconsistent with the levels observed in the solar wind at 1 AU and inferred for the high solar corona.

Applications of the simulation results and associated theory to type II and III bursts in the solar wind and corona, and to radiation from Earth's foreshock, suggest that LMC should produce both x- and o-mode radiation in these sources. Moreover, the production of both x- and o-mode radiation by LMC leads immediately to relatively weakly circularly polarized radiation, thereby immediately resolving the so-called "depolarization" problem for type III bursts without recourse to depolarization mechanisms outside the source. Of course, these may also operate too, either further depolarizing the radiation or alternatively (contrary to the standard picture) polarizing the radiation.

We calculated the total mode conversion efficiency ϵ into EM waves, as well as the separate conversion efficiencies into the o and x modes. The total conversion efficiencies depend on whether energy densities or power are considered, differing by the ratio of group speeds for the Langmuir/z and transverse waves. Total maximum conversion efficiencies for power are of order 70%, while those for energy density are of order 10%. Further reductions in efficiency result from averaging over the distributions of incident Langmuir wavevectors and gradient vectors of the density turbulence [25].

Both the conversion efficiencies into the o and x modes and the total conversion efficiency are strong functions of Ω and q, corresponding to the incidence angle of the Langmuir/z wave, normalized scale length of the density irregularity, and the normalized magnetic field strength. The conversion efficiencies into the o and x modes are almost equal in the unmagnetized regime (small Ω), only the o mode is produced at high enough Ω ($\gtrsim 1.5$), and the x mode dominates in an intermediate domain of Ω.

The presence of the magnetic field makes the mode conversion window's width in q, $\triangle q$, narrow with increasing Ω when $\Omega \approx 1$. A similar narrowing was predicted previously [19] for the inverse LMC process, in which radiation is converted into Langmuir/z waves. Moreover, the q-location of the peak efficiency varies with q as predicted by [19], again for the inverse problem. Interestingly, $\triangle q$ is approximately constant for $\Omega < 1$, contrary to the previous analytic prediction. It is plausible that this difference is due to WKB analyses breaking down for $\Omega \lesssim 1$, as found here in connection with interference effects.

A crucial new result is that the plasma magnetization causes the total conversion efficiency and the conversion efficiency into the o mode, but not the x mode, to oscillate strongly with increasing $\Omega \gtrsim 1$. These oscillations are well described semiquantitatively via a WKB-style analysis in terms of interference between ingoing and reflected Langmuir/z waves near the nominal mode conversion point. Moreover, the transmission factors from the

Langmuir/z mode to the o and x modes, again calculated via a WKB-style analysis, can explain semiquantitatively the almost equal conversion efficiencies into the o and x modes for small Ω and the rapid, monotonic decrease in the x-mode conversion efficiency for $\Omega \gtrsim 1$. In fact, the WKB-style analysis should break down for $\Omega \lesssim 1$, due to the characteristic distances (e.g., between the x- and o-mode cutoffs) no longer being large compared with relevant wavelengths, but it does provide results semiquantitatively consistent with the simulations. Future work should be directed at removing this issue.

Interestingly, for the inverse LMC process with incident o mode perpendicular to $\mathbf{B}_0$, Mjølhus [20] argued that the conversion efficiency should be a function of Ω and speculated that this might be due to an interference effect. Our analysis for LMC of incident Langmuir/z waves demonstrates the existence of such an interference effect, thereby providing indirect support for Mjølhus's speculation. Our simulation results show that LMC of Langmuir/z waves only produces o-mode waves for $\Omega \gg 1$. Thus in sufficiently strongly magnetized plasmas, such as the ionospheric context considered by Mjølhus, LMC will not produce x-mode waves.

In general the simulation results agree very well with previous simulations, numerical solutions, and analytic work (Figures 9-10 and Section IV.C. An exception is a discrepancy with approximate numerical solutions of the magnetized wave equations [16] where the power conversion efficiencies differ by a factor of 5 for the same value of Ω but different values of k_0L and plasma magnetization. The reason for the discrepancy is not known and should be addressed in future work. It may be due to neglect of interference effects in the numerical analysis or to approximations made there.

There are several limitations in this study. First, this paper considers the special case of $\nabla N_0 \parallel \mathbf{B}_0$ with arbitrary incidence angles for $\mathbf{K}$ relative to $\mathbf{B}_0$. However, preliminary results (not shown) confirm that the case studied here is not unusual: for oblique angles between ∇N_0 and $\mathbf{B}_0$, LMC produces x and o radiation with similar efficiencies.

Second, since the mode conversion efficiency ϵ is a function of q and Ω rather than k_0L, we use a single k_0L. For unmagnetized plasmas, our simulation results for the conversion efficiency ϵ show very good agreement with previous numerical and analytical results with different k_0L but the same q. However, the phase difference ϕ between incoming and reflected Langmuir/z waves in magnetized plasmas is a function of $\triangle Z = |Z_{\mathrm{mc}} - Z_{\mathrm{cut}}^z|$, which is related to k_0L. The interference pattern on $\Omega - q$ plane can thus be changed if k_0L varies and further studies of the effects of k_0L on ϵ in magnetized effects is needed.

Third, a higher level of β is assumed in the simulations than is appropriate to most plasmas. While we assumed typical parameters of f_p, f_{ce}, and k_0L in the solar wind at 1AU and the corona, values of $\gamma\beta \approx 10^{-2}$ were assumed to save computing time. However, comparisons of the simulations with previous results show that β effects

are relatively unimportant. This was also found for calculations of the transmission factors $\mathcal{A}^{mo}$, $\mathcal{A}^{ox}$, and $\mathcal{A}^{mx}$ and of the radiation's net polarization.

Fourth, as we mentioned before, a 1-D linear density gradient is assumed in the simulations and associated calculations. Other monotonic profiles are likely to yield semiquantitative differences, as found for instance by previously comparing LMC for linear versus parabolic profiles [24]. Qualitative differences can also occur: combining a linear density profile with superposed density fluctuations [37] yielded trapped modes and resonant variations in the conversion efficiency (e.g., increased efficiency when integer numbers of wavelengths fit within a cavity formed by the superposed turbulence). Thus, in order to consider the realistic characteristics of LMC in the solar wind and the corona, requires further investigation of the effects of L, β, superposed density fluctuations, and the angles between the incident wavevector, density gradient, and magnetic field.

In conclusion, we have presented numerical simulations of LMC between Langmuir/z and free-space o- and x-mode waves in warm magnetized plasmas and investigated possible applications of LMC to some solar system phenomena. We summarize the results as: (i) LMC can produce x-mode as well as o-mode radiation from Langmuir/z-mode waves. (ii) In the unmagnetized limit equal amounts of o- and x-mode radiation are produced and the total EM wave field changes from linear to circular polarization as B_0 and the magnetization parameter $\Omega \propto (k_0L)^{1/3}B_0^{1/2}$ increase. The radiation can has net circular polarization in the sense of the x mode for $0.5 \lesssim \Omega \lesssim 1.2$ and in the sense of the o mode for $\Omega \gtrsim 1.2$. (iii) The conversion efficiency into the x mode decreases monotonically as Ω increases while the o-mode conversion efficiency oscillates for $\Omega \gtrsim 0.5$. These oscillations are well modeled semiquantitatively for $\Omega \gtrsim 1$ as an interference phenomena between incoming and reflected Langmuir/z waves. (iv) Less than 10% of the incident Langmuir/z energy can be transformed into EM waves, although the corresponding power efficiencies differ by the ratio of the group speeds for each mode and are of order $50 - 70\%$. (v) The mode conversion window narrows as Ω increases for $\Omega \gtrsim 1$ (but is approximately constant for $\Omega \lesssim 1$) and the position of the peak agrees well with an analytic theory of Mjølhus. (vi) The transmission factor for Langmuir/z energy into the o and x modes is predicted and found to decrease with increasing q and Ω. Semiquantitative agreement with the simulations is found, explaining the equal transmission factors in the unmagnetized limit and the monotonic falloff of the x mode for $\Omega \gtrsim 1$. (vii) Propagation of the x mode inside the source region is shown to constrain the level of density fluctuations there. (viii) Standard parameters for the corona and the solar wind near 1 AU suggest that LMC should produce both o- and x- mode radiation for solar and interplanetary radio bursts and Earth's foreshock radiation. (ix) These results suggest that LMC can naturally explain the weak total circular polariza-

tions of coronal type II and III radio bursts in terms of the emission's intrinsic properties, resolving the "depolarization problem" without appeal to any depolarization mechanisms.

Acknowledgments

[1] T. H. Stix, *Waves in Plasmas* (American Institute of Physics, New York, 1992).
[2] K. G. Budden, *The Propagation of Radio Waves* (Cambridge Univ. Press, New York, 1985).
[3] D. B. Melrose, in *Solar Radiophysics: Studies of Emission From the Sun at Metre Wavelengths*, edited by D. J. McLean and N. R. Labrum, (Cambridge Univ. Press, New York, 1985), p. 177.
[4] E.-H. Kim, I. H. Cairns, and P. A. Robinson, Phys. Rev. Lett. **99**, 015003 (2007).
[5] L. Yin, M. Ashour-Abdalla, M. El-Alaoui, J. M. Bosqued, and J. L. Bougeret, Geophys. Res. Lett. **25**, 2609 (1998).
[6] I.H Cairns, J. Geophys. Res., **93**, 3958 (1988).
[7] R. P. Lin et al., Astrophys. J. **251**, 364 (1981).
[8] D. A. Gurnett, and W. S. Kurth, Space Sci. Rev. **78**, 53 (1996).
[9] P. H. Yoon et al., J. Geophys. Res. **103**, 29267 (1998).
[10] I. H. Cairns, S. Johnston, and P. Das, Mon. Not. R. Astron. Soc. **343**, 512 (2003).
[11] C. Rajyaguru et al., Phys. Rev. E **64**, 016403 (2001).
[12] K. L. McAdams, R. E. Ergun, J. LaBelle, Geophys. Res. Lett. **27**, 321 (2000).
[13] C. Rhodes et al., J. Appl. Phys. **100**, 054905 (2006).
[14] I. H. Cairns and D. B. Melrose, J. Geophys. Res. **90**, 6637 (1985)
[15] P. A. Robinson and I. H. Cairns, Solar Phys. **181**, 363 (1998).
[16] L. Yin and M. Ahour-Abdalla, Phys. Plasmas **6**, 449 (1999).
[17] D. W. Forslund et al., Phys. Rev. A **11**, 679 (1975).
[18] R. W. Means et al., Phys. Fluids **24**, 2197 (1981).
[19] E. Mjølhus, J. Plasma Phys. **30**, 179 (1983).
[20] E. Mjølhus, Radio Sci. **25**, 1321 (1990).
[21] A. J. Willes and I. H. Cairns, Publ. Aston. Soc. Aust. **18**, 355 (2001).
[22] K. Kim and D. -H. Lee, Phys. Plasmas **12**, 062101 (2005).
[23] D. E. Hinkel-Lipsker, B. D. Fried, and G. J. Morales, Phys. Fluids B **4**, 559 (1992).
[24] D. E. Hinkel-Lipsker, B. D. Fried, and G. J. Morales, Phys. Fluids B **4**, 1772 (1992).
[25] I. H. Cairns and A. J. Willes, Phys. Plasmas **12**, 052315 (2005).
[26] P. A. Robinson, I. H. Cairns, and A. J. Willes, Astrophys. J. **422**, 870 (1994).
[27] G. A. Dulk and S. Suzuki, Astron. Astrophys. **88**, 203 (1980).
[28] D. B. Melrose, *Plasma Astrophysics* (Gordon and Breach, New York, 1980).
[29] M. H. Cohen, Astrophys. J. **131**, 664 (1960).
[30] D. G. Wentzel, Solar Phys. **90**, 130 (1984).
[31] D. B. Melrose, Solar Phys. **119**, 143 (1989).
[32] D. B. Melrose, Astrophys. J. **637**, 1113 (2006).
[33] A. K. Ram and S. D. Schultz, Phys. Plasmas **7**, 4084 (2000).
[34] M. J. Reiner, J. Fainberg, M. L. Kiser, and J.-L. Bougeret, Solar Phys. **241**, 351 (2007).
[35] L. M. Celnikier, L. Muschietti, and M. V. Goldman, Astron. Astrophy **181**, 138 (1987).
[36] B. R. Bellamy, I. H. Cairns, and C. W. Smith, J. Geophys. Res. **110**, A10104 doi:10.1029/2004JA010952 (2005).
[37] A. J. Willes, S. D. Bale, and I. H. Cairns, J. Geophys. Res. **107**, 1320, 2002.

TABLE I: Typical parameters for the solar wind and the corona: ω_p, ω_p/ω_c, and $\langle L \rangle$ are from Ref. [15] while Ω is calculated from these using Eq. (8).

	ω_p (s^{-1})	ω_p/ω_c	$\langle L \rangle$	Ω
Solar wind at 1AU	1.5×10^5	100	1.3×10^6	0.87
Corona	1.5×10^8	10	60	0.98
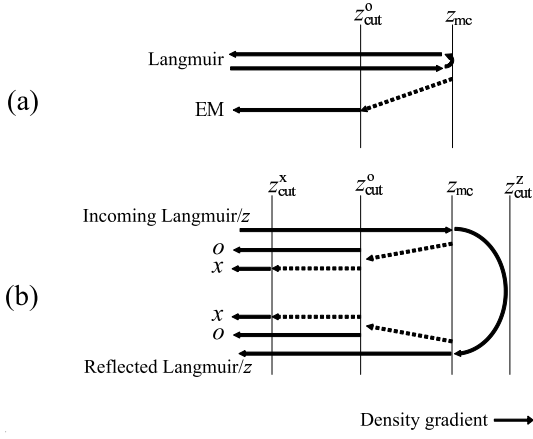
FIG. 1: Schematic illustration of mode conversion from Langmuir to electromagnetic waves in a linear density profile for (a) unmagnetized and (b) magnetized plasmas. Labels Z^o_{cut}, Z^x_{cut}, Z^z_{cut}, and Z_{mc} represent the position of the cutoffs of o-, x-, and Langmuir/z-modes, and the nominal mode conversion point, respectively. Dotted lines show possible connecting modes not present in a homogeneous plasma.
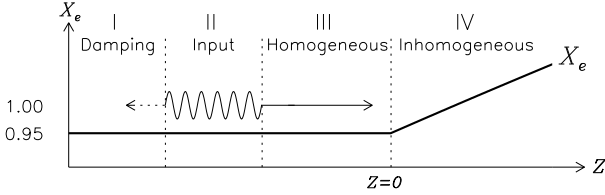
FIG. 2: Schematic illustration of simulation. Langmuir waves generated in Region II approach and encounter an increasing density gradient in Region III and IV. The plasma is assumed homogeneous in Region I-III and inhomogeneous in Region IV. Additional damping is imposed in Region I.
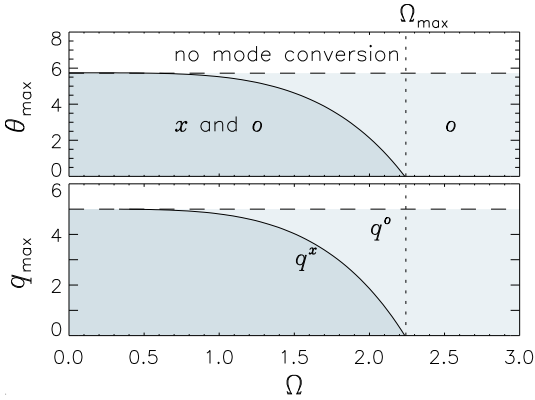
FIG. 3: (Top) The maximum angles $\theta^L = \theta^L_{max}$ and (bottom) maximum values of $q = q_{max}$ for LMC into the o (dashed line) and x (solid) as functions of Ω for $k_0 L = 1 \times 10^3$, $\gamma\beta = 0.01$, and $X_0 = 0.95$. The dark shaded region corresponds to LMC into both the o and x modes while the lightly shaded region corresponds to the o mode alone.
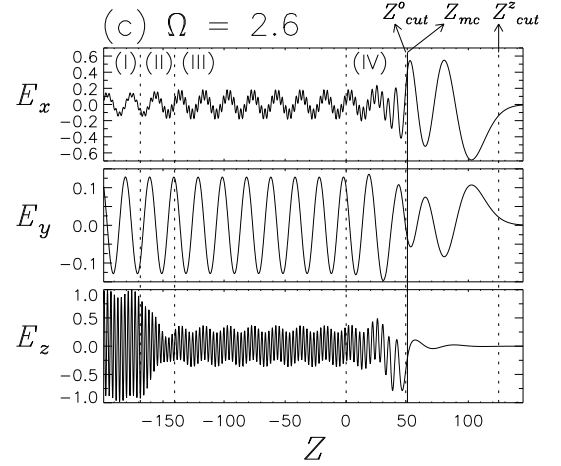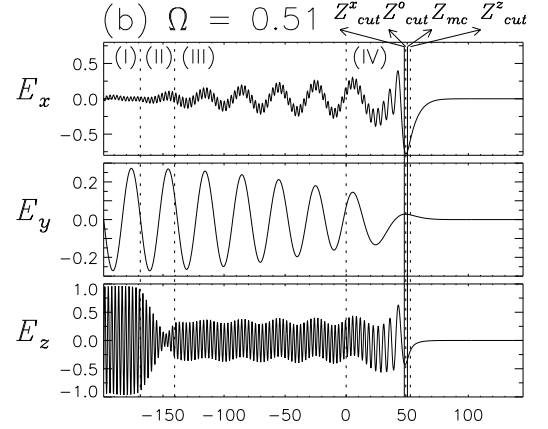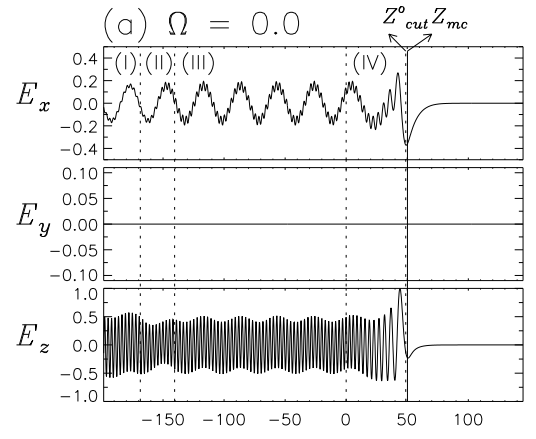
FIG. 4: Spatial dependence of the electric field along the direction of the inhomogeneity for $q = 0.5$, (a) $\Omega = 0.0$, (b) $\Omega = 0.51$, and (c) $\Omega = 2.6$. Here, the abscissa is the Z direction and the ordinate is the normalized electric amplitude in arbitrary units. Parameters are $X_0 = 0.95$, $\omega_{p0} = 2 \times 10^5$ s^{-1}, $k_0 L = 1 \times 10^3$, and $\gamma\beta = 0.01$.
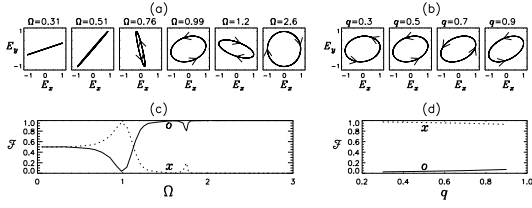
FIG. 5: Hodograms showing the polarization of the electric field transverse to $\mathbf{B}_0$ (i.e., E_X and E_Y) for (a) $q = 0.5$ and $\Omega = 0.31$, 0.51, 0.76, 0.99, 1.2, and 2.6, and (b) $\Omega = 0.99$ and $q = 0.3$, 0.5, 0.7, and 0.9. (c)-(d) Power fractions $\mathcal{F}$ of the o (solid line) and x (dotted) modes as functions of Ω for $q = 0.5$.
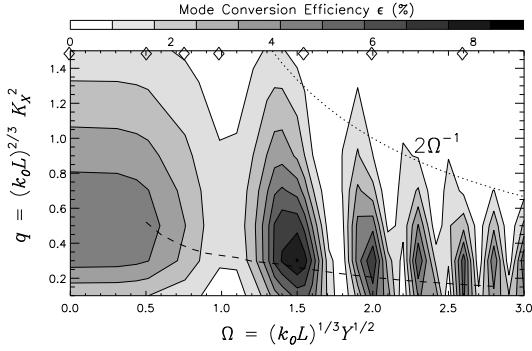
FIG. 6: Contour plot of the mode conversion efficiency ϵ in the q-Ω plane for $X_0 = 0.95$, $\omega_{p0} = 2 \times 10^5$ s^{-1}, $k_0 L = 1 \times 10^3$, and $\gamma\beta = 0.01$. Dotted and dashed lines show the relations $q = 2\Omega^{-1}$ and Eq. (25), respectively.
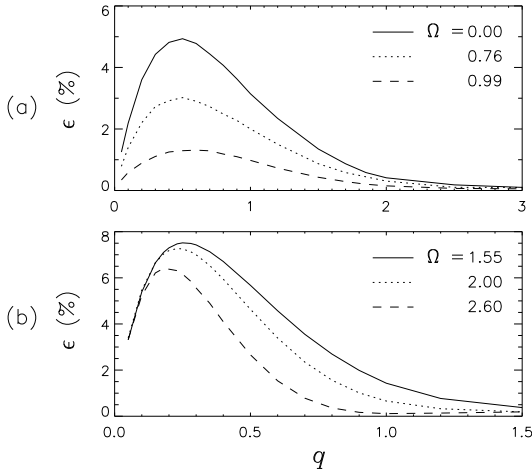
FIG. 7: Mode conversion efficiency ϵ versus q for (a) $\Omega < 1$ and (b) $\Omega > 1$. In (a), $\Omega = 0.0$ (solid line), 0.76 (dotted), and 0.99 (dashed). In (b), $\Omega = 1.55$ (solid), 2.0 (dotted), and 2.6 (dashed).
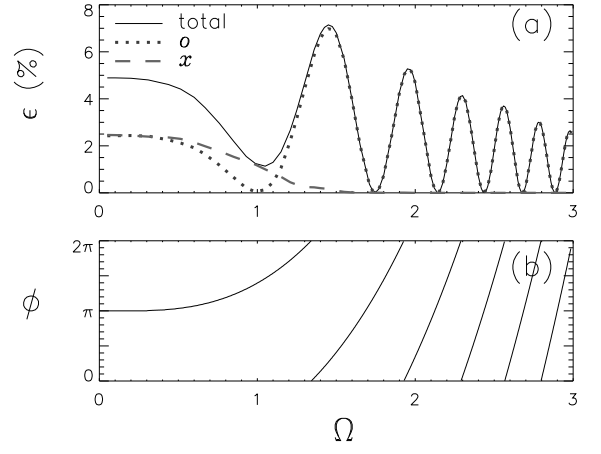
FIG. 8: (a) Conversion efficiency ϵ from Langmuir/z to both EM modes (solid line), the o mode (dotted), and the x mode (dashed) for $q = 0.5$. The values of X_0, $k_0 L$, and $\gamma\beta$ are as in Fig. 6. (b) Phase difference ϕ between incoming and reflected Langmuir/z modes vs Ω.
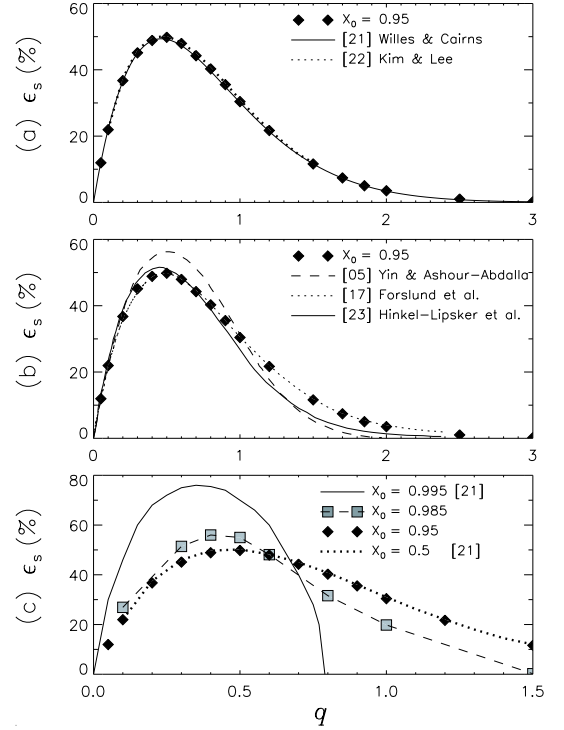
FIG. 9: Conversion efficiency ϵ_s given by Eq. (23) as a function of q in an unmagnetized plasma for various X_0. The parameters are $\omega_{p0} = 2 \times 10^5$ s^{-1}, $k_0 L = 1 \times 10^3$, $Y = 0$, and $\gamma\beta = 0.01$. The simulation results (diamonds) are compared with the numerical solutions of Ref. [17] and the approximate analytical results of Refs [16, 21–23].
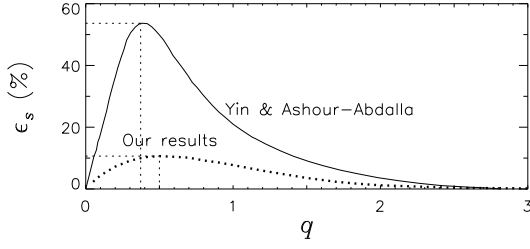
FIG. 10: Conversion efficiency ϵ_s given by Eq. (25) as a function of q. The dotted curve shows simulation results for $\Omega = 0.99$, $k_0 L = 1 \times 10^3$, $\gamma\beta = 1 \times 10^{-2}$, and $Y = 9.75 \times 10^{-3}$. The solid line shows Yin and Ashour-Abdalla's [16] results for $\Omega = 0.99$, $k_0 L = 192$, and $Y = 0.03$.
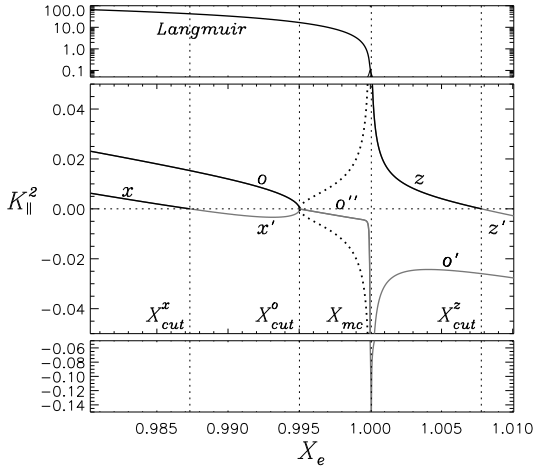

FIG. 13: (a) Values of q predicted by Eq. (35) for $\phi = 2\pi$ (diamond) and $\phi = \pi$ (circle) where ϕ is phase difference between incoming and reflected Langmuir/z modes. (b) Superposition of the predicted pattern of minima in ϵ onto Figure 6's simulation results.
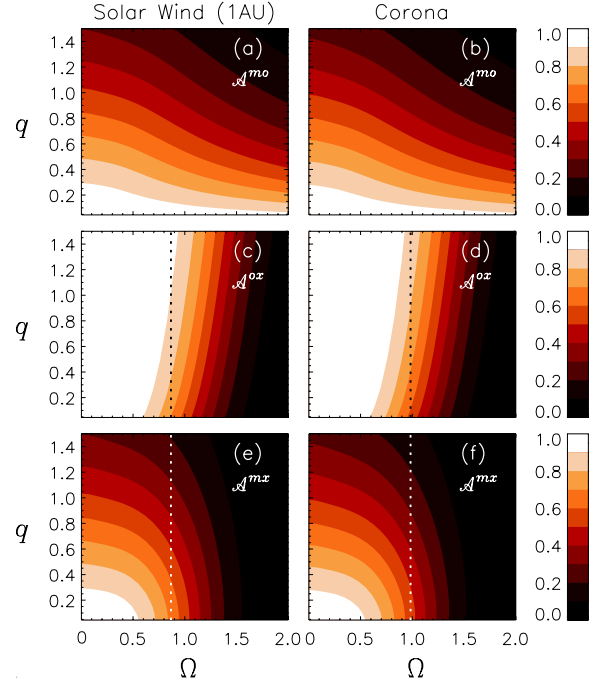

FIG. 11: Normalized squared wavenumber $K_\parallel^2$ parallel to $\mathbf{B}_0$ for the Langmuir/z, o and x modes as a function of $X_e = \omega_p^2/\omega^2$. Other parameters are $K_\perp = 0.7$, $\omega_p/\omega_c = 100$, and $\gamma\beta = 0.01$. Black and gray solid lines are positive and negative real solutions, respectively, and dotted lines represent imaginary solutions.
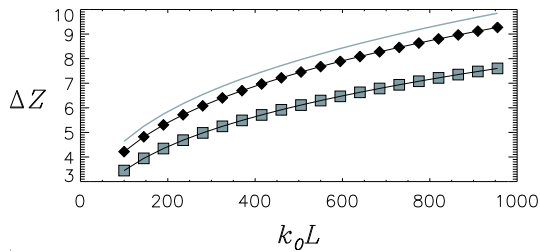
FIG. 12: Distance $\triangle Z$ between Z_{mc} and Z_{cut}^z for $\Omega = 1$, $X_0 = 0.95$: diamond and square symbols give the numerical predictions of Eq. (35) for $q = 0.1$ and 0.5, respectively, while the solid curve shows the approximation (36) for $K_X \ll 1$.

FIG. 14: (a)-(b) Transmission factors $\mathcal{A}^{mo}$ between Z_{mc} and Z_{cut}^o, (c)-(d) $\mathcal{A}^{ox}$ between Z_{cut}^o and Z_{cut}^x, and (e)-(f) $\mathcal{A}^{mx} = \mathcal{A}^{mo}\mathcal{A}^{ox}$ between Z_{mc} and Z_{cut}^x in the q-Ω plane. Panels (a), (c), and (e) are calculated for the solar wind at 1AU while panels (b), (d), and (f) correspond to the corona. Table I's values of ω_p and $k_0 L$ are used. Dotted lines represent $\Omega_{sw} = 0.87$ and $\Omega_{co} = 0.98$, respectively.
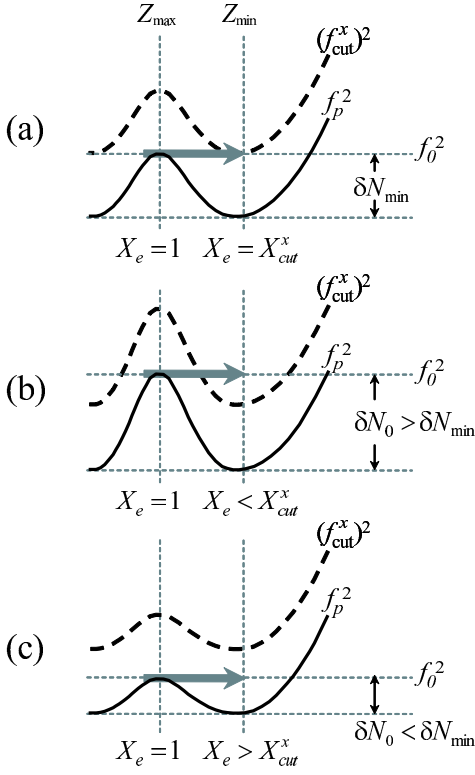
FIG. 15: The relationship between δN_0 and X_e: (a) $\delta N_0 = \delta N_{\min}$ and $X_e = X_{\mathrm{cut}}^x$ and (b) $\delta N_0 > \delta N_{\min}$ and $X_e < X_{\mathrm{cut}}^x$, so x-mode production is possible in a large regime, and (c) $\delta N_0 < \delta N_{\min}$ $X_e > X_{\mathrm{cut}}^x$, so x mode is not produced. The right arrow represents the incoming Langmuir wave. The solid and dashed curves are x-mode cutoff and local plasma frequencies, respectively.
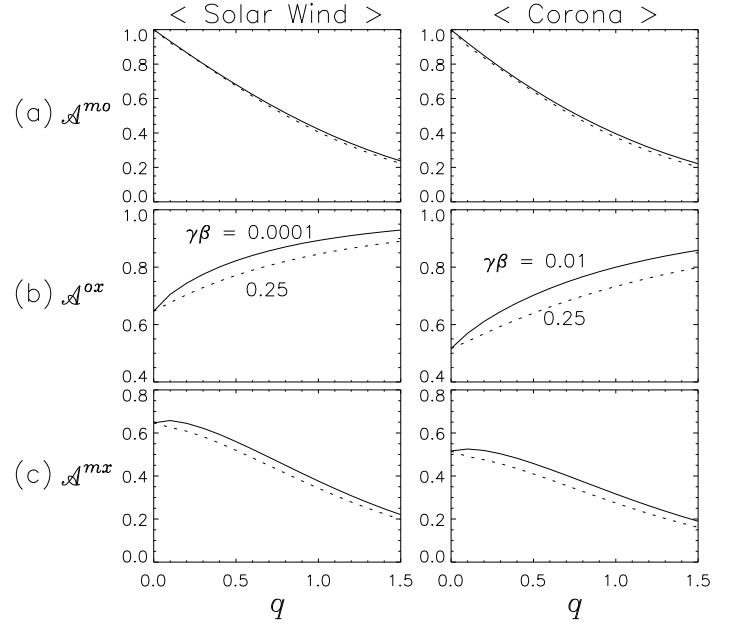

FIG. 16: Transmission factor (a) $\mathcal{A}^{mo}$, (b) $\mathcal{A}^{ox}$, and (c) $\mathcal{A}^{mx}$ at $\Omega_{sw} = 0.87$ for $\gamma\beta = 1 \times 10^{-4}$ (solid line) and 0.25 (dotted) in the solar wind at 1AU and at $\Omega_{co} = 0.98$ for $\gamma\beta = 0.01$ (solid) and 0.25 (dotted) in the solar wind at 1AU.
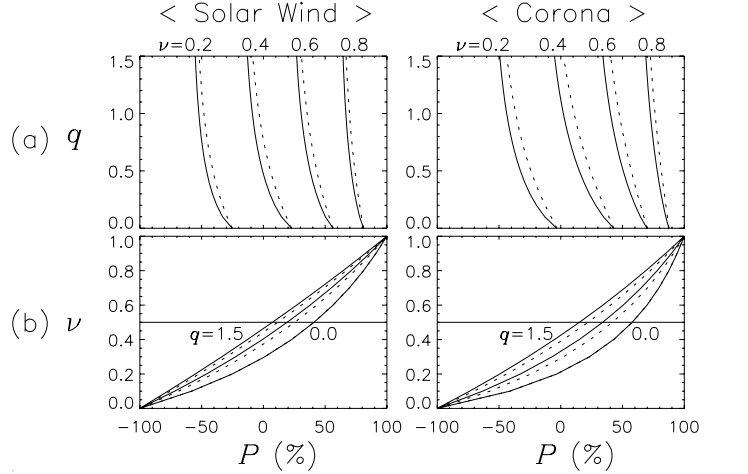

FIG. 17: Net degree of polarization as a function of (a) q for $\nu = 0.2$, 0.4, 0.6, and 0.8, and (b) ν for $q = 0.0$, 0.5, and 1.5, respectively. Left and right panels are for the nominal values of Ω in the solar wind (at 1 AU) and the corona, respectively. The solid lines are for $\gamma\beta = 10^{-4}$ (solar wind) and 0.01 (corona) and the dotted lines are both for $\gamma\beta = 0.25$.
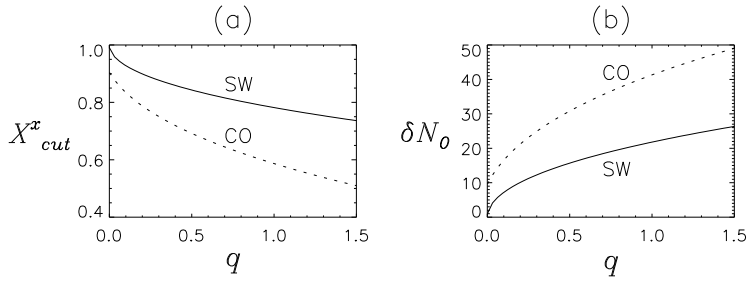
FIG. 18: The x-mode cutoff condition X_{cut}^x for the solar wind at 1AU and the corresponding constraints on δN_0. The shaded region is where the x mode propagates. The solid and dotted lines represent the nominal solar wind and corona, respectively.